A search for non-thermal radio emission from jets of massive young stellar objects

W. O. Obonyo,[1]⋆ S. L. Lumsden,[1]⋆ M. G. Hoare,[1]⋆ S. J. D. Purser [ORCID],[3] S. E. Kurtz[2] and K. G. Johnston[1]

[1]*School of Physics and Astronomy, The University of Leeds, Woodhouse Lane, Leeds LS2 9JT, UK*
[2]*Instituto de Radioastronomía y Astrofísica, Universidad Nacional Autónoma de México, Apartado Postal 3-72, Morelia 58089, México*
[3]*Astronomy & Astrophysics, Dublin Institute for Advanced Studies (DIAS), 10 Burlington Road, Dublin 4, Ireland*

ABSTRACT

Massive young stellar objects (MYSOs) have recently been shown to drive jets whose particles can interact with either the magnetic fields of the jet or ambient medium to emit non-thermal radiation. We report a search for non-thermal radio emission from a sample of 15 MYSOs to establish the prevalence of the emission in the objects. We used their spectra across the *L*, *C*, and *Q* bands along with spectral index maps to characterize their emission. We find that about 50 per cent of the sources show evidence for non-thermal emission with 40 per cent showing clear non-thermal lobes, especially sources of higher bolometric luminosity. The common or IRAS names of the sources that manifest non-thermal lobes are V645Cyg, IRAS 22134+5834, NGC 7538 IRS 9, IRAS 23262 + 640, AFGL 402d, and AFGL 490. All the central cores of the sources are thermal with corresponding mass-loss rates that lie in the range of $\sim 3 \times 10^{-7}$ to $7 \times 10^{-6} \, \mathrm{M_\odot \, yr^{-1}}$. Given the presence of non-thermal lobes in some of the sources and the evidence of non-thermal emission from some spectral index maps, it seems that magnetic fields play a significant role in the jets of massive protostars. Also noted is that some of the sources show evidence of binarity and variability.

Key words: stars: formation – stars: massive – stars: mass-loss – stars: protostars.

1 INTRODUCTION

Stellar jets and outflows are ever-present in both low- and high-mass young stellar objects (Anglada, Rodríguez & Carrasco-González 2018). They are detectable at radio wavelengths where the effect of dust extinction is minimal. Earlier observational studies of the jets from massive stars were limited to a few nearby objects e.g. HH 80-81 (Martí, Rodríguez & Reipurth 1998), Cepheus A HW2 (Curiel et al. 2006), IRAS 16547-4247 (Brooks et al. 2003), and G345.5 + 01.46 (Guzmán, Garay & Brooks 2010). However, with the upgrade of both the Australia Telescope Compact Array (ATCA) and the Very Large Array (VLA), it is now possible to study more distant objects in larger numbers. Such studies were conducted by Guzmán et al. (2012), Purser et al. (2016), Rosero et al. (2016), and Moscadelli et al. (2016) who confirmed that jets are ubiquitous in massive protostars. The jets are indicators of disc-fed accretion (Reipurth & Bally 2001), tracers of accretion history (Kuiper, Yorke & Turner 2015), and the vents through which part of the high radiation pressure from massive protostars are released (Kuiper et al.

2014; Banerjee & Pudritz 2007). They also remove excess angular momentum from the protostar to the ambient medium, allowing for further accretion (Anglada et al. 2018).

Models reveal a close connection between protostellar jets and accretion discs (Pudritz et al. 2007). This implies that the presence of a jet is an indicator of the existence of an accretion disc and vice versa. Indeed, a few massive young stellar objects (MYSOs) that drive jets are also known to harbour accretion discs e.g. IRAS 13481-6124 (Kraus et al. 2010, Caratti o Garatti et al. 2016), AFGL 2591 (Wang, van der Tak & Hogerheijde 2012), and G023.01-00.41 (Sanna et al. 2019). These discs, if optically thick, might explain how the objects accrete mass in the presence of high radiation pressure and strong UV fields (Vaidya, Fendt & Beuther 2009).

Typically, an MYSO is understood to consist of a central object, a disc and a jet. However, it is only the jet that is expected to emit non-thermal radiation (Velusamy, Langer & Marsh 2007; López-Cámara & Raga 2010; Carrasco-González et al. 2013). Charged jet particles can be accelerated (Bell 1978; Blandford & Eichler 1987) to relativistic levels at shocks where they may interact with magnetic fields giving rise to non-thermal (synchrotron) emission. The shocks are therefore traced by the non-thermal radio knots and

⋆ E-mail: pywoo@leeds.ac.uk (WOO); s.l.lumsden@leeds.ac.uk (SLL); m.g.hoare@leeds.ac.uk (MGH)

Table 1. Table showing object names, pointing centres, distance from the Sun, and Bolometric luminosities as taken from the Urquhart et al. (2011) catalogue. Local rms noise levels of the maps and properties of their restoring beams (size in arcsec and position angle in degrees) at *L* band are also shown.

RMS name	Common Name	RA (J2000)	Dec. (J2000)	d (kpc)	L_{bol} ($L_\odot$)	Field rms (μJy beam^{-1})	Beam size maj (arcsec) × min (arcsec)	PA (°)
G083.7071+03.2817	–	20^{h}33^{m}36^{s}51	+45°35′44″0	1.4	3900	25	1.45 × 1.13	83.0
G094.2615−00.4116	IRAS 21307+5049	21^{h}32^{m}30^{s}59	+51°02′16″0	5.2	9000	33	1.47 × 1.09	82.3
G094.4637−00.8043	IRAS 21334+5039	21^{h}35^{m}09^{s}14	+50°53′08″9	4.9	21000	25	1.47 × 1.11	82.6
G094.6028−01.7966	V645Cyg	21^{h}39^{m}58^{s}25	+50°14′20″9	4.9	43000	24	1.49 × 1.13	83.1
G103.8744+01.8558	IRAS 22134+5834	22^{h}15^{m}08^{s}97	+58°49′07″3	1.6	6800	23	1.53 × 1.08	78.2
G108.5955+00.4935C	IRAS 22506+5944	22^{h}52^{m}38^{s}09	+60°01′01″1	4.3	3000	17	1.30 × 1.10	− 26.7
G110.0931−00.0641	IRAS 23033+5951	23^{h}05^{m}25^{s}16	+60°08′15″4	4.3	11850	18	1.31 × 1.16	− 19.8
G111.2552−00.7702	IRAS 23139+5939	23^{h}16^{m}10^{s}40	+59°55′28″2	3.5	9870	18	1.39 × 1.20	− 22.9
G111.5671+00.7517	NGC 7538 IRS 9	23^{h}14^{m}01^{s}76	+61°27′19″9	2.7	44620	29	1.32 × 1.22	− 17.9
G114.0835+02.8568	IRAS 23262+6401	23^{h}28^{m}27^{s}76	+64°17′38″5	4.2	7130	20	1.33 × 1.06	− 13.5
G126.7144−00.8220	S187 IR	01^{h}23^{m}33^{s}17	+61°48′48″2	0.7	2600	20	1.47 × 1.06	− 25.1
G136.3833+02.2666	IRAS 02461+6147	02^{h}50^{m}08^{s}57	+61°59′52″1	3.2	7800	40	1.50 × 1.15	− 05.1
G138.2957+01.5552	AFGL 402d	03^{h}01^{m}31^{s}32	+60°29′13″2	2.9	17000	25	1.45 × 1.12	25.8
G139.9091+00.1969A	AFGL 437s	03^{h}07^{m}24^{s}52	+58°30′43″3	3.2	11000	25	1.29 × 1.06	21.2
G141.9996+01.8202	AFGL 490	03^{h}27^{m}38^{s}76	+58°47′00″1	0.8	5500	28	1.30 × 1.06	27.4

Herbig-Haro (HH) objects. Some of the theories put forward to explain how shocks are formed in YSOs include episodic accretion (DeSouza & Basu 2015) and interaction between jet material with the ambient medium and/or internal working surfaces within the jet (Rubini et al. 2007). Star formation models that incorporate discs can explain how the shocks are formed in MYSOs. For instance, an unstable self-gravitating disc can fragment into clumps that are accreted episodically towards a protostar, causing accretion bursts (Meyer et al. 2017). Similarly, a wobbling magnetized disc has a potential of producing knots at working surfaces (Raga, Kofman & Falle 1993) if jet material spirals through its hourglass-like field lines (Blandford & Payne 1982; Pudritz & Norman 1986; Pudritz & Banerjee 2005). Recent observations of HH 80-81 (Rodríguez-Kamenetzky et al. 2017; Vig et al. 2018) and the triple radio source in the Serpens star-forming region (Rodríguez-Kamenetzky et al. 2016) have confirmed that massive protostars emit both thermal and non-thermal radiation. They used spectral indexing to classify the emissions. The study by Vig et al. (2018) demonstrated the value of studying the spectral index for non-thermal emission at lower radio frequencies.

Unlike thermal jets and outflows that have been well modelled (Reynolds 1986), models of non-thermal jets can be improved with an increase in observational data. Numerical simulations can also be used to provide clues on how both magnetohydrodynamic (MHD) and radiative-hydrodynamic (RHD) jets (de Gouveia Dal Pino 2005) are launched, accelerated, and collimated. In-depth, study of the objects can reveal whether they represent different evolutionary phases. Claims have been made that an MYSO can drive either an MHD jet e.g. HH 80-81 (Carrasco-González et al. 2010), an RHD jet e.g. W75N(B) (Carrasco-González et al. 2015), or an RHD equatorial wind e.g. S140 IRS 1 (Hoare 2006).

Motivated by the need to establish the prevalence of non-thermal emission in protostellar jets, we observed a sample of MYSOs at *L* band (frequency range 1–2 GHz and central frequency 1.5 GHz) where synchrotron emission is dominant and easily detectable. We also used previous *C*- and *Q*-band observations from the Jansky Very Large Array (JVLA)'s A configuration by Purser et al. (in preparation). The *C*- and *Q*-band observations were of bandwidths 2 and 8 GHz, centred at 6 and 44 GHz, respectively.

2 SAMPLE SELECTION

A total of 15 objects (listed in Table 1) were selected from a sample of 63 MYSOs that were previously observed in *C* band at 6 GHz using the NRAO's[1] JVLA telescope (details in Purser et al., in preparation). We selected the 15 brightest objects from that sample to provide the best possibility for detection in *L* band at 1.5 GHz.

The 15 objects chosen are all from the RMS catalogue[2] (Lumsden et al. 2013). Other selection criteria include a distance $d \lesssim 7$ kpc from the Sun and bolometric luminosities $L_{bol} \gtrsim 2500 \, L_\odot$. Given that the typical sizes of MYSO jets lie in the range of ∼0.1 –2.4 pc (Mundt & Ray 1994), we should resolve some of the lobes within the jets at the frequency of observation and telescope configuration (i.e. resolution of 1.2 arcsec).

3 OBSERVATIONS AND DATA REDUCTION

The 15 objects were observed on 2015 August 8, 19, and 22 using the JVLA under project code 15A-218. The observation made use of 27 antennae of the A configuration giving a resolution θ_{HPBW} of ∼1.2 arcsec at the central frequency of *L* band. The continuum data were subdivided into 16 spectral windows (SPW), each of bandwidth 64 MHz. The spectral windows were further subdivided into 64 channels, each of width 1 MHz to ease flagging procedure and control the spread of RFI across the observed frequencies. The sources observed at *L* band were also observed at *C* band in 2012 and some of them at *Q* band in 2014/15 (Purser et al., in preparation) using the JVLA's A configuration. Synthesized beams of *C* and *Q* bands are typically 0.33 and 0.04 arcsec, respectively. Noise levels in *C*- and *Q*-band maps lie in the range ∼6.5–10 μJy beam^{-1} and ∼35–60 μJy beam^{-1} at full uv-range, i.e. 13–800 and 100–5300 kλ, respectively.

The *L*-band sources were observed with a phase calibrator cycle time of ∼3–7 min to correct for instrumental and atmospheric effects on their phases and flux densities. Each of the science objects had a total integration time of ∼30–40 min. Flux calibrators

[1] National Radio Astronomy Observatory
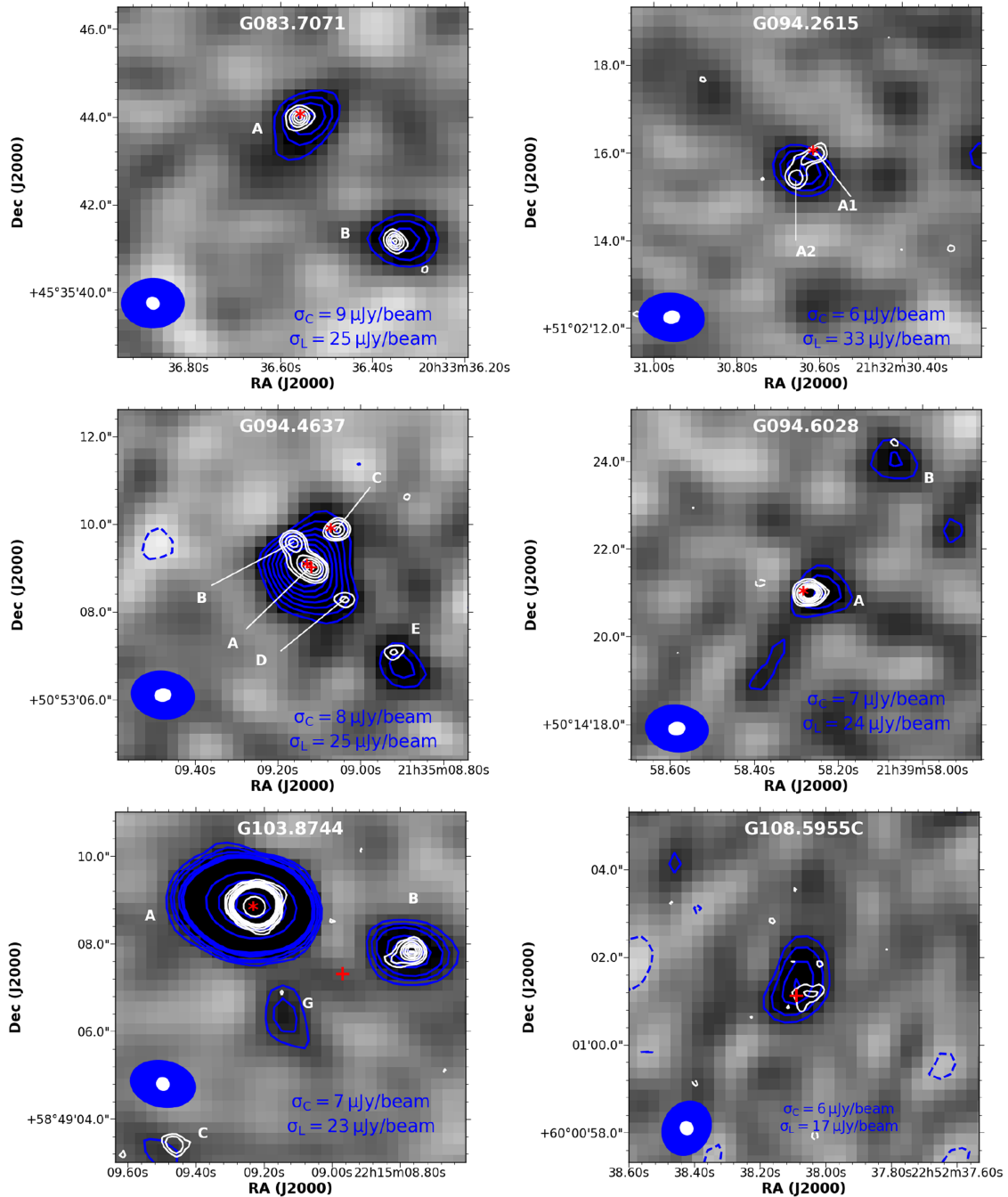[2] http://rms.leeds.ac.uk/cgi-bin/public/RMS_DATABASE.cgi

Figure 1. *L*-band maps of the sources together with their *L*- and *C*-band contours of levels -3σ (dashed), 3σ, 4σ, 5σ, ..., and -3σ (dashed), 3σ, 5σ, 9σ, 13σ, 17σ, 21σ, ... shown in blue and white colours, respectively. All the cores were detected at *L* band except for G138.2957 and G136.3833, both of which were detected at *C* band. The red asterisks show the *Q*-band locations of the MYSOs' cores. The locations agree with the positions of the IR emission from the MYSOs within 1 arcsec. IR locations of MYSOs whose Q-band positions are unavailable are indicated with a plus sign. Synthesized beams for both *L* and *C* bands (Purser et al., in preparation) are shown in the lower left corner of each frame.

$0137 + 331 = 3C48$ and $1331 + 305 = 3C286$ were also observed for flux scaling.

Calibration and imaging were done using NRAO's CASA (Common Astronomy Software Applications; McMullin et al. 2007). If an image had a bright object in its field, a phase-only self-calibration of between one and three iterations was carried out to improve it. While CLEANing the data, their *uv* visibilities were weighted using Briggs weighting with a robustness parameter of 0.5 (Briggs 1995), resulting in synthesized beams whose average sizes are ~1.4 arcsec × 1.1 arcsec. The rms noise levels of the cleaned maps of full *uv*-coverage, ~ 2–220 kλ, lie in the range 18–40 μJy beam^{-1} with objects close to bright and extended sources having higher rms noise. A list showing the objects, their local rms noise and sizes of synthesized beams used in deconvolution is shown in Table 1.
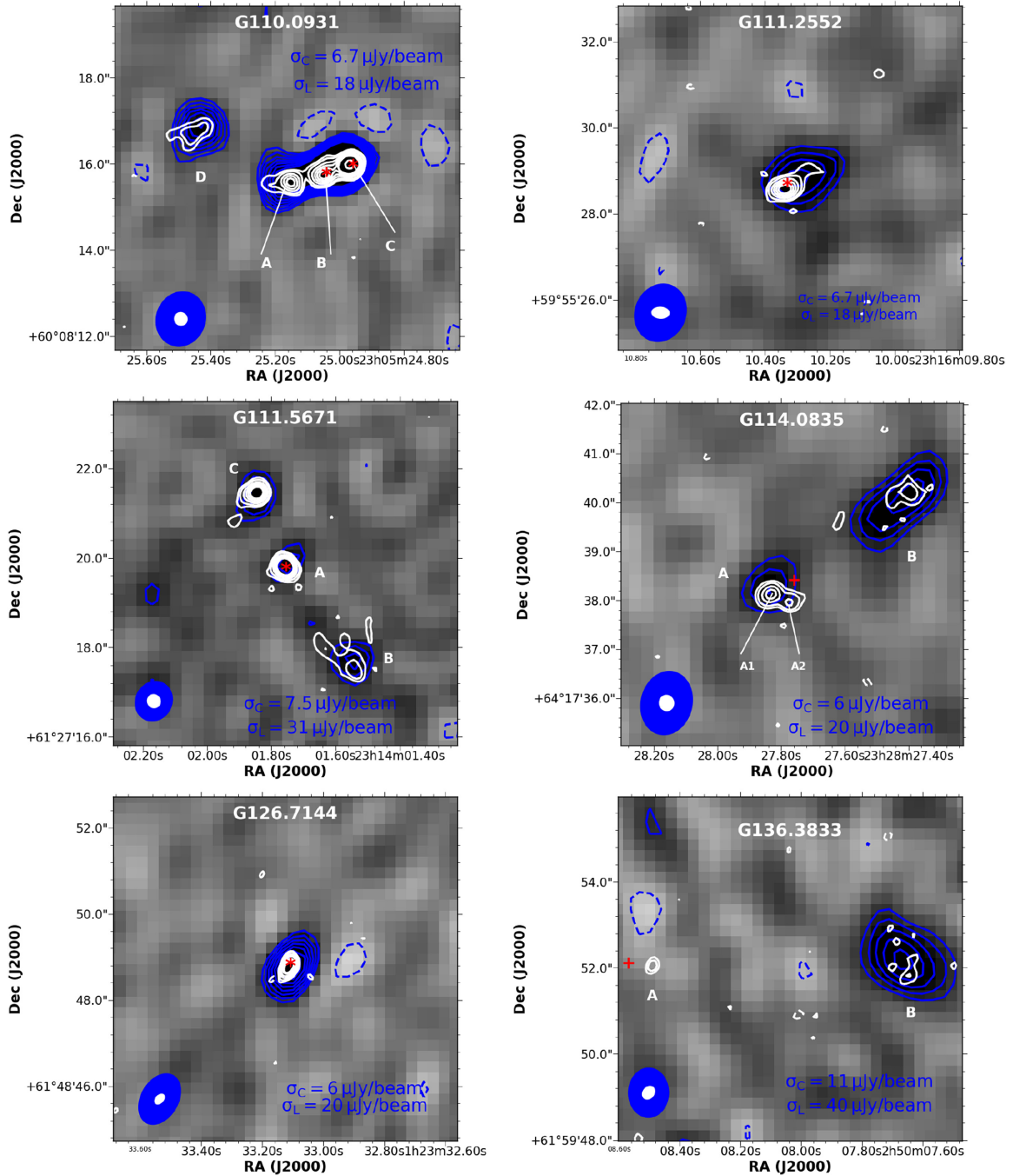
Figure 1. Fig. 1 - *continued*.

4 NEAR INFRARED EMISSION

Massive protostars are embedded in natal clouds containing dust particles that can be distributed into various geometries by jets and outflows from the protostars, creating cavities and shells within the clouds. Light from the embedded sources can then scatter off the dust in the cavities at near infrared (NIR) wavelengths, tracing their structure. Molecular hydrogen emission at 2.12 µm from shocks produced by jets are also seen. As a result, infrared images were relied upon to provide helpful hints for the presence of protostellar outflows and jets.

Most of the infrared images used in the study were generated by the Wide Field Camera (WFCAM; Casali et al. 2007) of the United Kingdom Infra-red Telescope (UKIRT; Lawrence et al. 2007) as part of the UKIDSS Galactic Plane Survey (Lucas et al. 2008). UKIRT is a 3.8-m telescope whose typical angular resolution is ~0.8 arcsec (Lucas et al. 2008). WFCAM, whose pixel scale is 0.4 arcsec, observes at five IR wave bands: *Z, Y, J, H,* and *K* of wavelength range of 0.83–2.37 µm. Only three of the bands *J, H,* and *K* of central wavelengths 1.2483, 1.6313, and 2.2010 µm, respectively (Hewett et al. 2006), were used in the study. In addition, Two
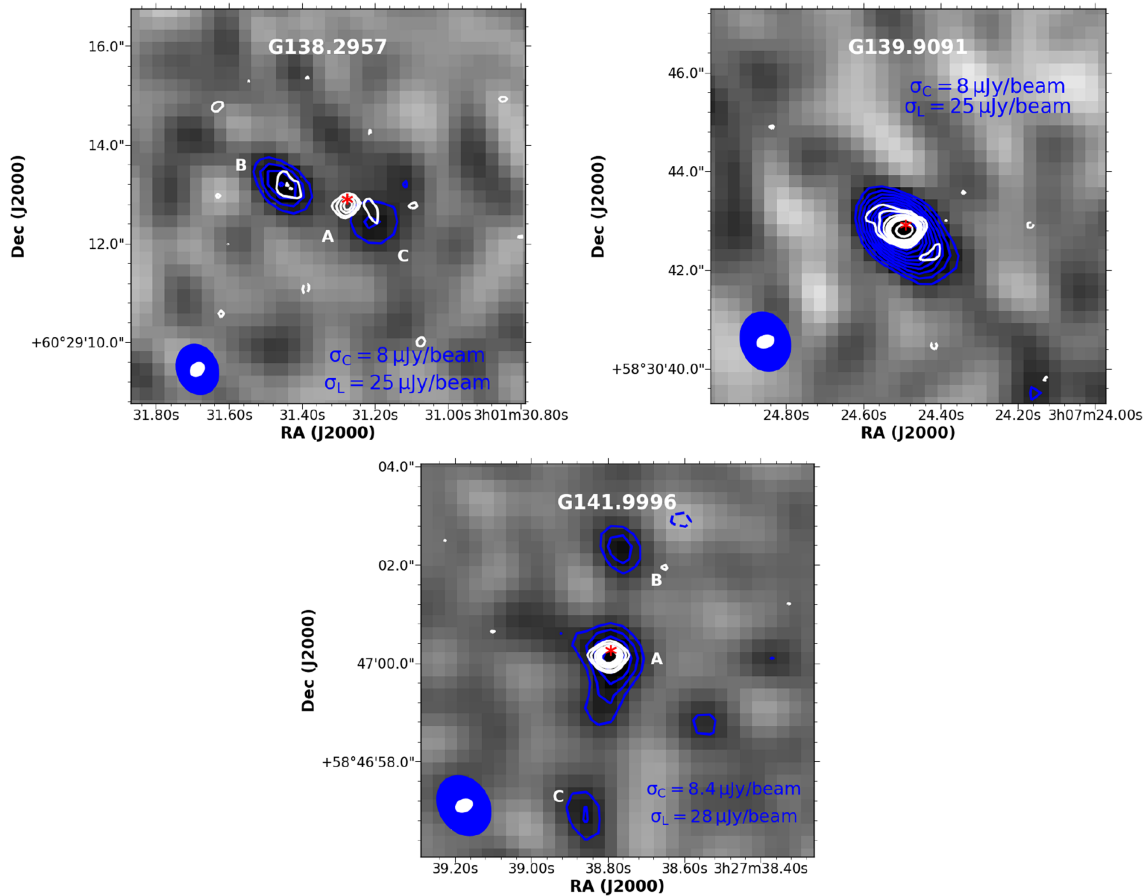
Figure 1. Fig. 1 - *continued*.

Micron All Sky Survey (2MASS) images of some of the objects were inspected, especially if their declinations are above the region of the sky covered by UKIDSS i.e. $\delta > 60°$, even-though the images are of a lower resolution ($\sim$2.5 arcsec) and sensitivity i.e. a pixel size of 2 arcsec (Skrutskie et al. 2006). Also used were findings from H_2 emission observations of the MYSOs, e.g. Navarete et al. (2015), Wolf-Chase, Arvidsson & Smutko (2017), Varricatt et al. (2010), and Davis et al. (1998).

5 RESULTS AND DISCUSSION

5.1 *L*-band results

L-band images of all the sources are shown in Fig. 1. Positions, fluxes, sizes, and position angles of all their components are presented in Table 2. The components can be classified as cores or lobes. A core is detectable in the near/mid-infrared, brighter at higher radio frequencies, e.g. *Q* band, and is likely to be located between lobes, if the components show a linear orientation. Lobes, on the other hand, are seen a few arc-seconds away from the cores, aligned in the direction of the outflow cavities. Thermal lobes are detectable at higher frequencies while non-thermal lobes are more prominent at lower radio frequencies.

The L-band images display a variety of morphologies ranging from emission that comes from cores with radio lobes and partially resolved cores to point-like counterparts. G094.4637, G094.6028, G111.5671, G114.0835, G138.2957, and G141.9996 have radio lobes, suggesting that they harbour cores that drive

the jets. G110.0931, on the other hand, is resolved, displaying an extended and jet-like structure but does not have radio lobes at *L* band. However, it encloses multiple components at higher resolution in *C* band. Some of the components may be lobes. Other sources whose *L*-band emission encloses multiple components at the higher resolution, in *C* band, are G094.2615, G094.4637, and G139.9091. Four sources G083.7071-A, G108.5955C, G111.2552, and G139.9091 are partially resolved, while three G103.8744-A, G114.0835-A, and G126.7144 are point-like.

The cores of all the protostars were detected at *L* band except for G103.8744, G136.3833, and G138.2957. None of the detections in the field of G103.8744 appear to be its core; they are all located a few arcseconds away from the position of the MYSO. G136.3833's field has a bright source that is approximately 6 arcsec to the west. This source does not manifest an explicit association with the MYSO. G138.2957, on the other hand, has two non-thermal lobes that are approximately 2 arcsec apart. Each of the lobes are located $\sim$1 arcsec away from the position of the core (see Fig. 1). All the *L*- and *C*-band emissions have a positional match that agree within $\sim$0.3 arcsec. However, NIR positions, taken from 2MASS, show slight offsets from the radio emission, perhaps because the emission is from a section of an outflow cavity that is further away from the source and is less obscured. In some cases, no radio emission coincides with the NIR position e.g. G103.8744 where the peak of the radio sources are positioned a few arcseconds away from the peak of the IR emission.

The flux densities and peak fluxes of the sources that lie within a radius of 5–10 from the MYSOs' position were estimated by

Table 2. A table showing the position, flux density, peak flux, size, and position angle of emission from the components of the MYSOs at *L* band. Sources whose sizes are not shown are point like at the resolution of 1.2 arcsec. Any other sources that are located near an MYSO and are likely to be associated with it are also listed. The source naming scheme is adopted from Purser et al. (in preparation) for consistency.

Object Name	RA (J2000)	Dec. (J2000)	Integrated Flux (mJy)	Peak flux (mJy)	Deconvolved source size θ_{maj}(arcsec) $\times$ θ_{min}(arcsec)	Position angle (°)
G083.7071-A	20^{h}33^{m}36^{s}56	+45°35′43″9	0.17 ± 0.02	0.13 ± 0.02	2.4 ± 0.2 × 1.6 ± 0.3	130 ± 10
G083.7071-B	20^{h}33^{m}36^{s}34	+ 45°35′41″1	0.09 ± 0.02	0.09 ± 0.03	–	–
G094.2615(A1 + A2)	21^{h}32^{m}30^{s}61	+ 51°02′15″8	0.11 ± 0.02	0.13 ± 0.03	2.0 ± 0.3 × 1.1 ± 0.2	48 ± 7
G094.4637(A+B+C+D)	21^{h}35^{m}09^{s}13	+ 50°53′09″1	0.38 ± 0.04	0.27 ± 0.03	1.8 ± 0.4 × 1.6 ± 0.4	–
G094.4637-E	21^{h}35^{m}08^{s}91	+ 50°53′07″0	0.03 ± 0.01	0.04 ± 0.02	–	–
G094.6028-A	21^{h}39^{m}58^{s}27	+ 50°14′20″9	0.08 ± 0.02	0.12 ± 0.02	–	–
G094.6028-B	21^{h}39^{m}58^{s}07	+ 50°14′24″0	0.07 ± 0.02	0.10 ± 0.02	–	–
G103.8744-A	22^{h}15^{m}09^{s}25	+ 58°49′08″8	2.21 ± 0.10	1.90 ± 0.05	3.3 ± 0.3 × 2.3 ± 0.2	70 ± 15
G103.8744-B	22^{h}15^{m}08^{s}79	+ 58°49′07″8	0.17 ± 0.02	0.23 ± 0.02	2.3 ± 0.2 × 1.3 ± 0.2	63 ± 16
G103.8744-G	22^{h}15^{m}09^{s}16	+ 58°49′06″6	0.09 ± 0.03	0.15 ± 0.02	–	–
G108.5955C	22^{h}52^{m}38^{s}06	+ 60°01′01″1	0.20 ± 0.03	0.16 ± 0.02	1.9 ± 0.4 × 1.1 ± 0.3	160 ± 20
G110.0931	23^{h}05^{m}25^{s}04	+ 60°08′15″8	0.59 ± 0.08	0.38 ± 0.04	2.6 ± 0.3 × 1.2 ± 0.2	108 ± 8
G110.0931-D	23^{h}05^{m}25^{s}43	+ 60°08′16″9	0.19 ± 0.03	0.17 ± 0.03	–	–
G111.2552	23^{h}16^{m}10^{s}34	+ 59°55′28″6	0.16 ± 0.03	0.12 ± 0.02	1.7 ± 0.5 × 1.1 ± 0.4	121 ± 11
G111.5671-A	23^{h}14^{m}01^{s}76	+ 61°27′19″8	0.12 ± 0.03	0.17 ± 0.02	–	–
G111.5671-B	23^{h}14^{m}01^{s}54	+ 61°27′17″5	0.20 ± 0.03	0.17 ± 0.03	–	–
G111.5671-C	23^{h}14^{m}01^{s}85	+ 61°27′21″4	0.18 ± 0.03	0.18 ± 0.03	–	–
G114.0835-A	23^{h}28^{m}27^{s}82	+ 64°17′38″1	0.10 ± 0.03	0.10 ± 0.01	–	–
G114.0835-B	23^{h}28^{m}27^{s}40	+ 64°17′40″2	0.21 ± 0.04	0.13 ± 0.02	2.5 ± 0.4 × 1.2 ± 0.3	135 ± 8
G126.7144	01^{h}23^{m}33^{s}11	+ 61°48′48″8	0.47 ± 0.05	0.56 ± 0.03	2.0 ± 0.2 × 1.2 ± 0.3	140 ± 15
G136.3833-A	02^{h}50^{m}08^{s}49	+ 61°59′52″1	<0.01	<0.12	–	–
G136.3833-B	02^{h}50^{m}07^{s}68	+ 61°59′52″2	0.65 ± 0.05	0.29 ± 0.01	1.6 ± 0.4 × 0.8 ± 0.3	60 ± 12
G138.2957-A	03^{h}01^{m}31^{s}28	+ 060°29′12″8	<0.06	<0.06	–	–
G138.2957-B	03^{h}01^{m}31^{s}45	+ 060°29′13″2	0.13 ± 0.04	0.16 ± 0.02	1.5 ± 0.2 × 0.8 ± 0.2	48 ± 8
G138.2957-C	03^{h}01^{m}31^{s}20	+ 060°29′12″4	0.10 ± 0.03	0.12 ± 0.02	–	–
G139.9091	03^{h}07^{m}24^{s}49	+ 58°30′42″8	0.41 ± 0.04	0.34 ± 0.02	2.5 ± 0.3 × 1.5 ± 0.2	50 ± 8
G141.9996-A	03^{h}27^{m}38^{s}76	+ 58°47′00″2	0.31 ± 0.04	0.18 ± 0.02	2.3 ± 0.5 × 1.6 ± 0.3	180 ± 21
G141.9996-B	03^{h}27^{m}38^{s}77	+ 58°47′02″3	0.06 ± 0.03	0.12 ± 0.02	–	–
G141.9996-C	03^{h}27^{m}38^{s}86	+ 58°46′57″0	0.07 ± 0.03	0.11 ± 0.02	–	–

enclosing a box around a source. Uncertainties on the fluxes were calculated by averaging fluxes from five different locations of a source's field that were devoid of emission, estimated using a box of the same size. An additional error, approximated at 10 per cent of a source's flux density was incorporated, in quadrature, to include the uncertainty associated with calibration of absolute flux. Sizes of the sources θ_S were calculated as $\theta_S = \sqrt{\theta_{FWHM}^2 - \theta_B^2}$, where θ_S is the deconvolved size of the source, θ_{FWHM} is the full-width at half maximum of a source's flux distribution and θ_B is the full width at half maximum of the beam. These quantities, together with their position angles, calculated by inspection, are presented in Table 2. A source's radio emission was considered real if its peak flux is at least three times higher than the root mean square noise in the field (i.e. at least 3σ detection). Sources were considered resolved if their structures are extended with respect to the beam (i.e. larger than the beam) otherwise they are compact.

5.2 Spectral indices and maps of the sources

Spectral indexing provides a means of classifying radio emitters as either thermal ($\alpha \geq -0.1$) or non-thermal ($\alpha < -0.1$) e.g. Rodríguez-Kamenetzky et al. (2017), Vig et al. (2018). However, it is difficult to distinguish between optically thin thermal emission and non-thermal emission if the value of the spectral index is closer to -0.1 and the uncertainties are large. Non-thermal emission is thus

claimed with certainty only when $\alpha << -0.1$ and the uncertainty on the index does not allow for overlap with -0.1.

The integrated fluxes of the sources at *L*, *C*, and *Q* bands, together with any others available in literature, were used to estimate their indices despite the fact that data collection was not contemporaneous and MYSOs may be variable e.g. S255 NIRS 3 (Cesaroni et al. 2018). Moreover, the observations are of different resolutions and are clearly sensitive to different spatial scales. To ensure the accuracy of the method, both *L*- and *C*-band data were re-imaged using a common range of uv-wavelength i.e. 15–200 kλ, so as to use emissions from comparable spatial scales in estimating the spectral indices of the sources. None the less, full range of uv-wavelength was used in *Q* band despite the fact that it traces a different spatial scale since the overlap between its uv-coverage and 15–200 kλ is insufficient. Further caution was exercized by estimating *L*- and *C*-band fluxes from a similar enclosing box regardless of the morphology of a source to provide for uniformity.

A high-resolution observation at *Q*-band can result in missing flux (van der Tak & Menten 2005), but at the same time dust emission contribute about 43±11 per cent (Purser 2017) of the flux at *Q* band. For example, the flux of G111.5671 at 44 GHz (Purser et al., in preparation), observed using the VLA's A configuration is lower than C-configuration flux (van der Tak & Menten 2005) by 18 per cent. Thus, the quantities of free–free emission at *Q* band, essential for estimating the spectral indices, are unknown and some of the indices may have large uncertainties. However, the indices
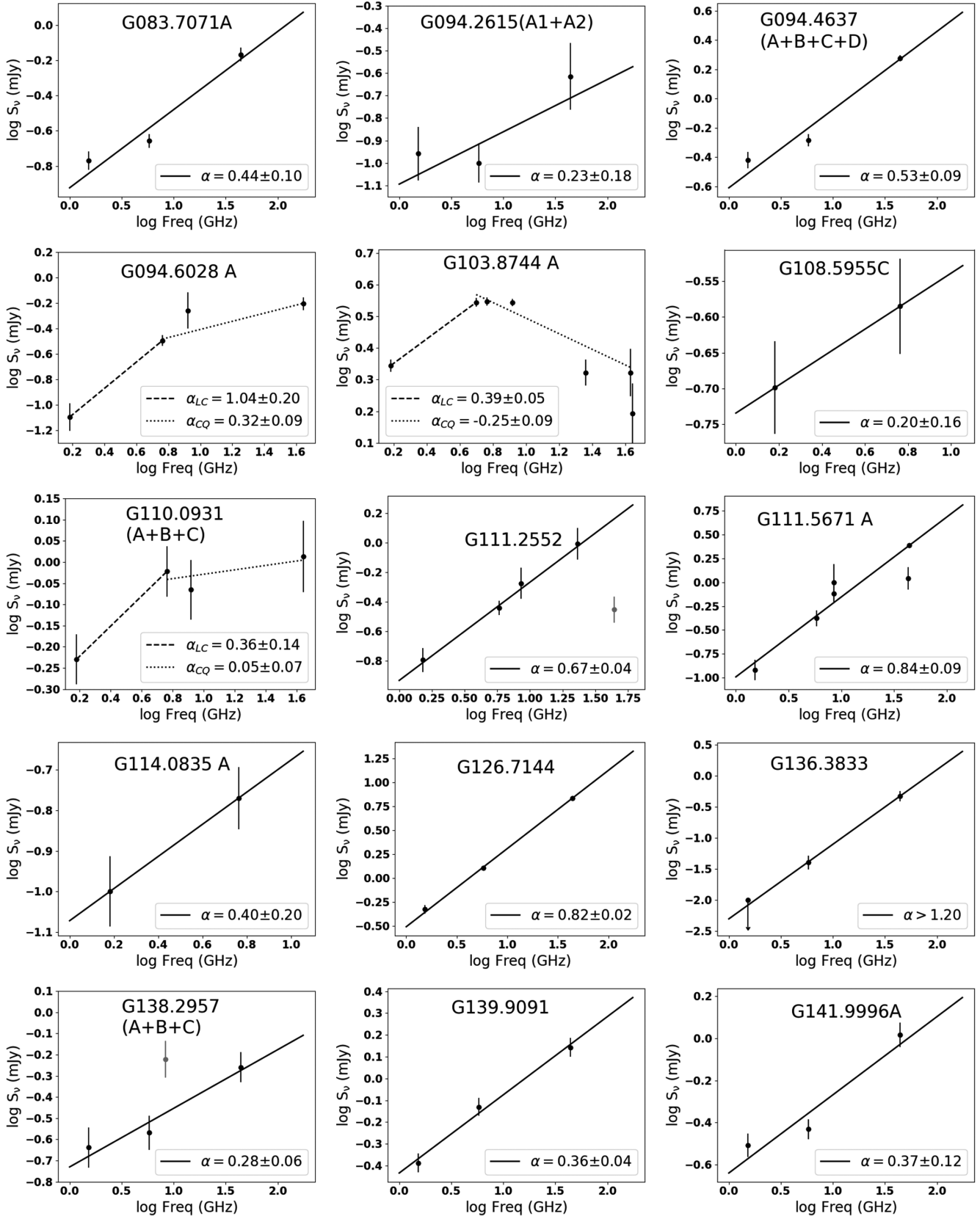
Figure 2. A plot showing how flux density of the sources at *L* band, which harbour cores, varies, with frequency. The radio emission of the MYSO, G103.8744 was not detected and the spectrum of a H II region that is closest to its location was used. In some sources, additional data, available in the literature and listed in Table 3, were used in estimating the indices. The red data points represent values that were considered to be too low or high due to variability and were not used in the fit.

Table 3. Flux densities of the objects at different frequencies together with their spectral indices. Both *L*- and *C*-band fluxes shown are from images of similar range of uv-distance (in λ). The Q-band fluxes were taken from Purser et al. (in preparation). For fluxes taken from literature, the reference is shown in brackets. Separable components of the MYSOs are also included in the table. The class tells whether an *L*-band emission traces a core or a lobe. Known H II regions, assumed to be sources that have stopped driving jets, are also indicated in the table.

Object	Integrated flux (mJy)				Spectral index			Class
	1.5 GHz	5.8 GHz	44.0 GHz	Other (Ref)	α_{LC}	α_{CQ}	α_{LQ}	
G083.7071-A	0.17 ± 0.02	0.22 ± 0.02	0.68 ± 0.06	–	0.19 ± 0.11	0.56 ± 0.06	0.44 ± 0.10	Core
G083.7071-B	0.09 ± 0.02	0.20 ± 0.02	–		0.60 ± 0.13	–	–	Core
G094.2615(A1+A2)	0.11 ± 0.03	0.10 ± 0.02	0.24 ± 0.08		-0.07 ± 0.25	0.44 ± 0.20	0.23 ± 0.18	Core/Lobe
G094.4637(A+B+C + D)	0.38 ± 0.04	0.52 ± 0.05	1.89 ± 0.08		0.23 ± 0.12	0.64 ± 0.05	0.53 ± 0.09	Core(s) + lobe(s)
G094.4637-E	0.03 ± 0.01	0.04 ± 0.02	–	–	0.21 ± 0.45	–	–	Lobe
G094.6028-A	0.08 ± 0.02	0.32 ± 0.03	0.62 ± 0.07	(a)	1.04 ± 0.20	0.32 ± 0.09	0.44 ± 0.15	Core
G094.6028-B	0.07 ± 0.02	<0.04	–		<-0.42	–	–	Lobe
G103.8744-A	2.21 ± 0.10	3.52 ± 0.04	1.56 ± 0.34	(f)	0.39 ± 0.05	-0.25 ± 0.06	–	H II region
G103.8744-B	0.17 ± 0.02	0.25 ± 0.06	<0.11	–	0.29 ± 0.20	–	–	Unknown
G103.8744-C	<0.06	0.09 ± 0.02	–	–	>0.30	–	–	Unknown
G103.8744-G	0.09 ± 0.03	<0.05	–	–	<-0.44	–	–	Lobe
G108.5955C	0.20 ± 0.03	0.26 ± 0.04	–	–	0.20 ± 0.16	–	–	Unknown
G110.0931(A+B + C)	0.59 ± 0.08	0.95 ± 0.13	1.03 ± 0.20	(b)	0.36 ± 0.14	0.05 ± 0.07	0.17 ± 0.07	Core + lobe(s)
G110.0931-A	–	0.22 ± 0.02	–	(b)	–	-0.14 ± 1.49	–	Lobe
G110.0931-B	–	0.31 ± 0.02	0.62 ± 0.15	(b)	–	0.33 ± 0.14	–	Core
G110.0931-C	–	0.49 ± 0.01	0.38 ± 0.11	(b)	–	-0.11 ± 0.07	–	Unknown
G110.0931-D	0.19 ± 0.03	0.17 ± 0.02	–	–	-0.08 ± 0.15	–	–	H II region
G111.2552	0.16 ± 0.03	0.36 ± 0.04	0.35 ± 0.07	(c)	0.61 ± 0.16	0.73 ± 0.08	0.67 ± 0.04	Core
G111.5671-A	0.12 ± 0.03	0.42 ± 0.08	2.46 ± 0.10	(d)	0.94 ± 0.23	0.79 ± 0.14	0.84 ± 0.09	Core
G111.5671-B	0.20 ± 0.03	<0.09	–	–	<-0.60			Lobe
G111.5671-C	0.18 ± 0.03	0.40 ± 0.09	–	–	0.60 ± 0.21	–	–	Lobe
G114.0835-A	0.10 ± 0.03	0.17 ± 0.03	–	–	0.40 ± 0.20	–	–	Core
G114.0835-B	0.21 ± 0.04	0.12 ± 0.02	–	–	-0.42 ± 0.19	–	–	Lobe
G126.7144	0.47 ± 0.05	1.28 ± 0.05	6.86 ± 0.24	–	0.75 ± 0.08	0.83 ± 0.02	0.82 ± 0.02	Core
G136.3833-A	<0.01	0.04 ± 0.01	0.47 ± 0.09	–	>1.04	1.22 ± 0.16	>1.20	Core
G136.3833-B	0.65 ± 0.05	0.26 ± 0.02	<0.14	–	-0.68 ± 0.08	<-0.31	<-0.49	Unknown
G138.2957(A+B+C)	0.23 ± 0.05	0.27 ± 0.05	0.55 ± 0.09	(e)	0.12 ± 0.15	0.35 ± 0.09	0.28 ± 0.06	Core + lobes
G138.2957-B	0.13 ± 0.04	–	–	–	–	–	–	Lobe
G138.2957-C	0.10 ± 0.03	–	–	–	–	–	–	Lobe
G139.9091	0.41 ± 0.04	0.74 ± 0.07	1.39 ± 0.14	–	0.44 ± 0.10	0.31 ± 0.07	0.36 ± 0.04	Core
G141.9996-A	0.31 ± 0.04	0.37 ± 0.04	1.04 ± 0.14	–	0.13 ± 0.13	0.51 ± 0.09	0.37 ± 0.12	Core
G141.9996-B	0.06 ± 0.03	<0.03	–	–	<-0.51	–	–	Lobe
G141.9996-C	0.07 ± 0.03	<0.03	–	–	<-0.63	–	–	Lob

References: (a) – Di Francesco et al. (1997).

(b) – Rodríguez, Trinidad & Migenes (2012).

(c) – Trinidad et al. (2006).

(d) – Sandell, Goss & Wright (2005).

(e) – Carral et al. (1999).

(f) – Wang et al. (2016).

are used since the SEDs of most of the cores, shown in Fig. 2, do not show a strong evidence of unexpected behaviour.

The indices were estimated to be equivalent to the slopes of the lines of best fit of a plot of logarithm of flux density and frequency of an object, generated by minimizing chi-squares (shown in Fig. 2). In cases where a source's flux density could not be estimated (i.e too faint to detect), an upper limit, evaluated as three times its field rms (i.e. $3 \times$ rms) was set as its peak flux. An upper limit on the integrated flux of such a source was estimated from a polygon whose size is similar to that of the source at a frequency where it is detected. Some sources are extended at *L* band but are resolved into multiple cores and lobes e.g. G094.4637 or a core and a lobe e.g. G094.2615 in the higher resolution *C* and *Q* bands. For the extended sources, the flux at *L* band and the sum of the fluxes of the components in the higher resolution observations were used to estimate the index. Indices of the resolved components, on the other hand, were estimated from the fluxes at the frequencies where they are resolved. If a source was

only detected at one frequency, a limit on the index was calculated. Table 3 shows a list of the objects, their spectral indices and the fluxes used in estimating the indices. Details of the components incorporated in the calculation of the spectral indices of *L*-band sources that harbour multiple components are indicated in Table 3.

Spectral index maps of the MYSOs were generated from *L*- and *C*-band images using CASA task immath in spix mode to display the distribution of the indices across a source. The maps used are of *uv*-wavelength range of 15–200 kλ. Only pixels whose values are more than 3σ in both *L* and *C* bands were used in creating the maps. The re-imaged C-band maps show varied morphologies, some of which are comparable to *L*-band emission e.g. G110.0931 while others are not e.g. G111.2552 and G108.5955 (see Fig. 3). Uncertainty in the spectral index of a given pixel on the map was approximated by assuming that the error on the flux of each cell is equivalent to the rms of the field. This error was propagated while calculating the spectral index of corresponding *L*- and *C*-
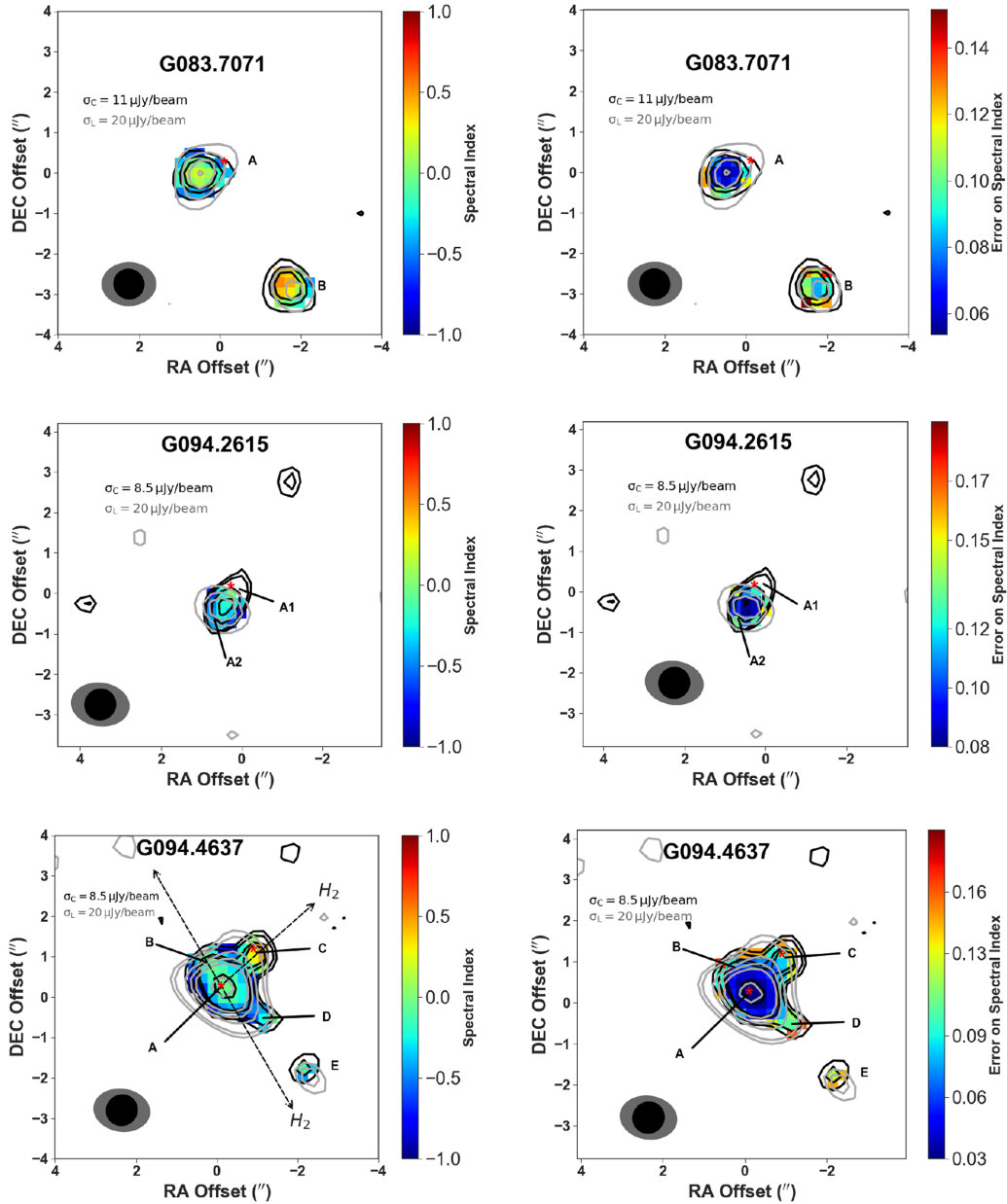
Figure 3. Spectral index maps of the sources shown on the left-hand panels and their corresponding error maps on the right. *L*- and *C*-band contours of levels 3, 5, 7σ, ... and 3, 7, 11, 15σ, ... are overlaid in grey and black colours, respectively. The maps were generated from *L*- and *C*-band maps of similar uv-wave coverage (i.e. 15–200 kλ). Colour scales show *L–C* band spectral indices α_{LC} of the sources and corresponding errors. Locations of sources that lie within the *L*-band emission are indicated by their names. The dashed lines are the approximate directions of known emissions that are associated with outflows. Asterisk and plus symbols are the *Q* band and IR locations of the MYSO cores. The synthesized beams are shown in the lower left corner.

band pixels. The maps and the corresponding errors are shown in Fig. 3. Whereas the beams of *L*- and *C*-band maps that were used in generating the spectral index maps are largely similar, a few maps were generated from *C*-band images of smaller beams. The smaller *C*-band beams can result in slightly lower fluxes at *C* band and more negative spectral indices on the pixels of non-thermal sources.

5.2.1 Spectral indices of the cores

The *L–Q* band spectral indices α_{LQ} show that all the detected cores are thermal radio emitters ($\alpha > -0.1$). To decipher the nature of

the objects further, their *L*-, *C*- and *Q*-band fluxes, among others from the literature, were used to compare their spectral indices as derived from *L* to *C* bands α_{LC} with those from *C* to *Q* bands α_{CQ}. Table 3 shows three possibilities: α_{LC} that is lower than α_{CQ} e.g. G094.2615, G094.4637, and G141.9996; α_{LC} that is higher than α_{CQ} e.g. G110.0931 and G094.6028-A, and α_{LC} which is comparable to α_{CQ} e.g. G139.9091 and G126.7144.

Sources whose $\alpha_{LC} < \alpha_{CQ}$ have overall spectral indices that are flattened by *L*-band fluxes. This may be due to steepening of α_{CQ} by dust emission at *Q* band or contribution of non-thermal emission at *L* band. Purser (2017) estimated that dust emission is, on average, $\sim 43 \pm 11$ per cent of the total emission at 44 GHz, capable of
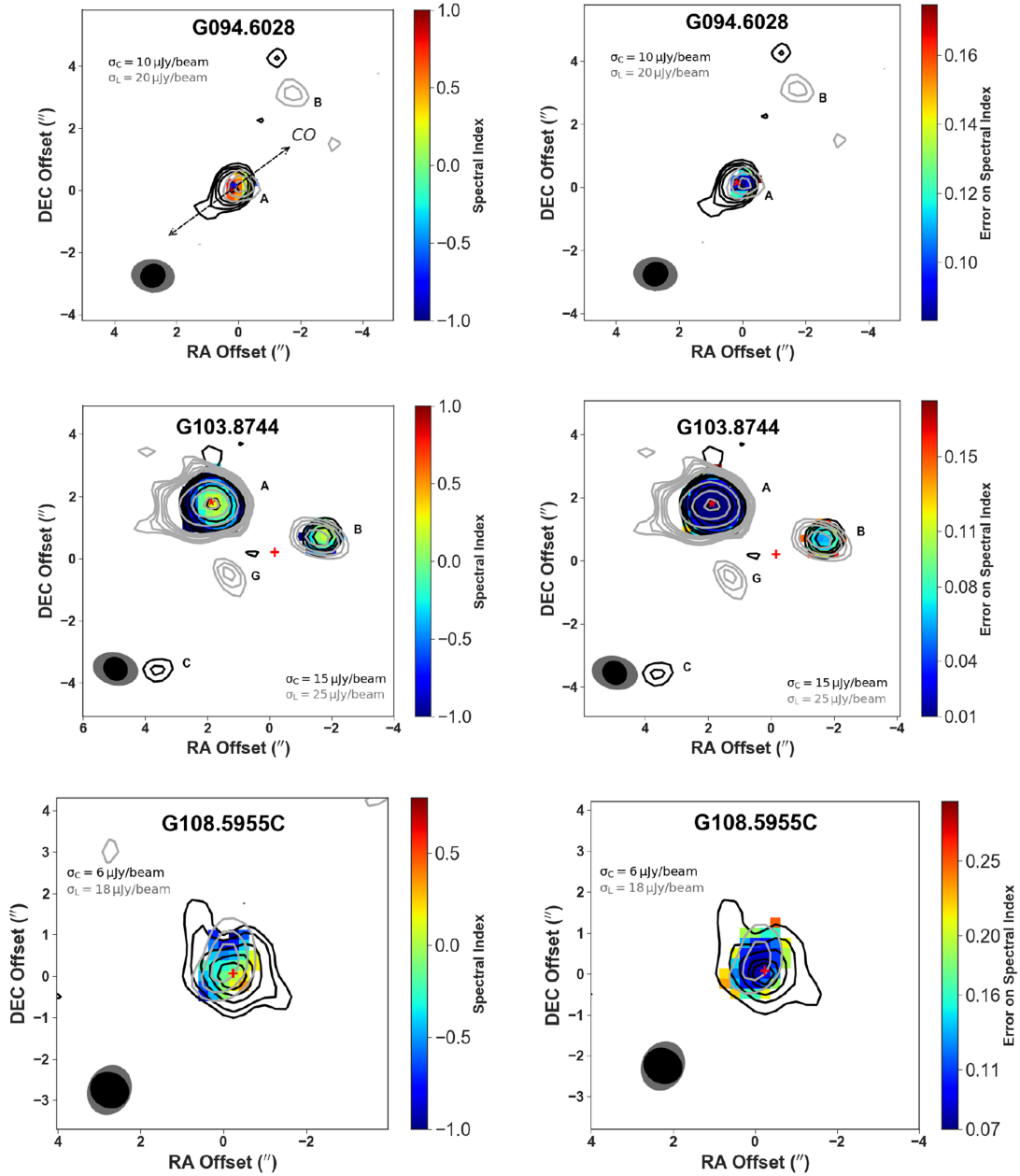
Figure 3. *- continued.*

steepening C–Q band slope; however, the values of α_{CQ} are $\sim$+0.6, consistent with thermal jets.

Spectra of sources whose α_{LC} are higher than α_{CQ} exhibit an H II region-like feature due to the apparent turnovers of their SEDs. In G110.0931, this can clearly be attributed to loss of flux at Q band where one of its components (A) was not detected. Finally, sources whose α_{LC} are comparable with α_{CQ} seem to have thermal cores that are separated from the lobes (e.g. in G111.5671-A) or cores with no clear lobes (e.g. in G111.2552 and G126.7144). In conclusion, L–Q band spectral indices (α_{LQ}) of the MYSOs are largely positive ($\alpha >$ 0) and the radiation from what one can consider a central component of a MYSO is also primarily thermal, making it a substantial radio emitter at higher frequencies. The average α_{LC}, α_{CQ}, and α_{LQ} of the sources are 0.42 ± 0.34, 0.43 ± 0.33, and 0.42 ± 0.27 confirming that the cores are thermal.

5.2.2 Spectral indices of lobes

Four sources, G094.6028, G103.8744, G111.5671, and G141.9996, have non-thermal lobes of spectral indices $\alpha \leq -0.42$. The lobes were detected at L band but not C band. G138.2957 has non-thermal lobes of spectral indices -0.46 ± 0.31 and -0.38 ± 0.33 to the east and west of its thermal core, respectively (see Fig. 3). Two sources G114.0835 and G136.3833 have nearby non-thermal sources that are aligned with the orientation of NIR emission in their fields. G094.4637 has a thermal lobe whose L- and C-band emissions are displaced in the direction of the outflow. It also has a component D that is non-thermal. Besides the lobes, two sources G094.2615 and G108.5955 show tentative indications of non-thermal emission to the south-east and east of their cores, respectively.

These findings suggest that six of the sources, equivalent to 40 per cent, have non-thermal lobes that indicate the presence of
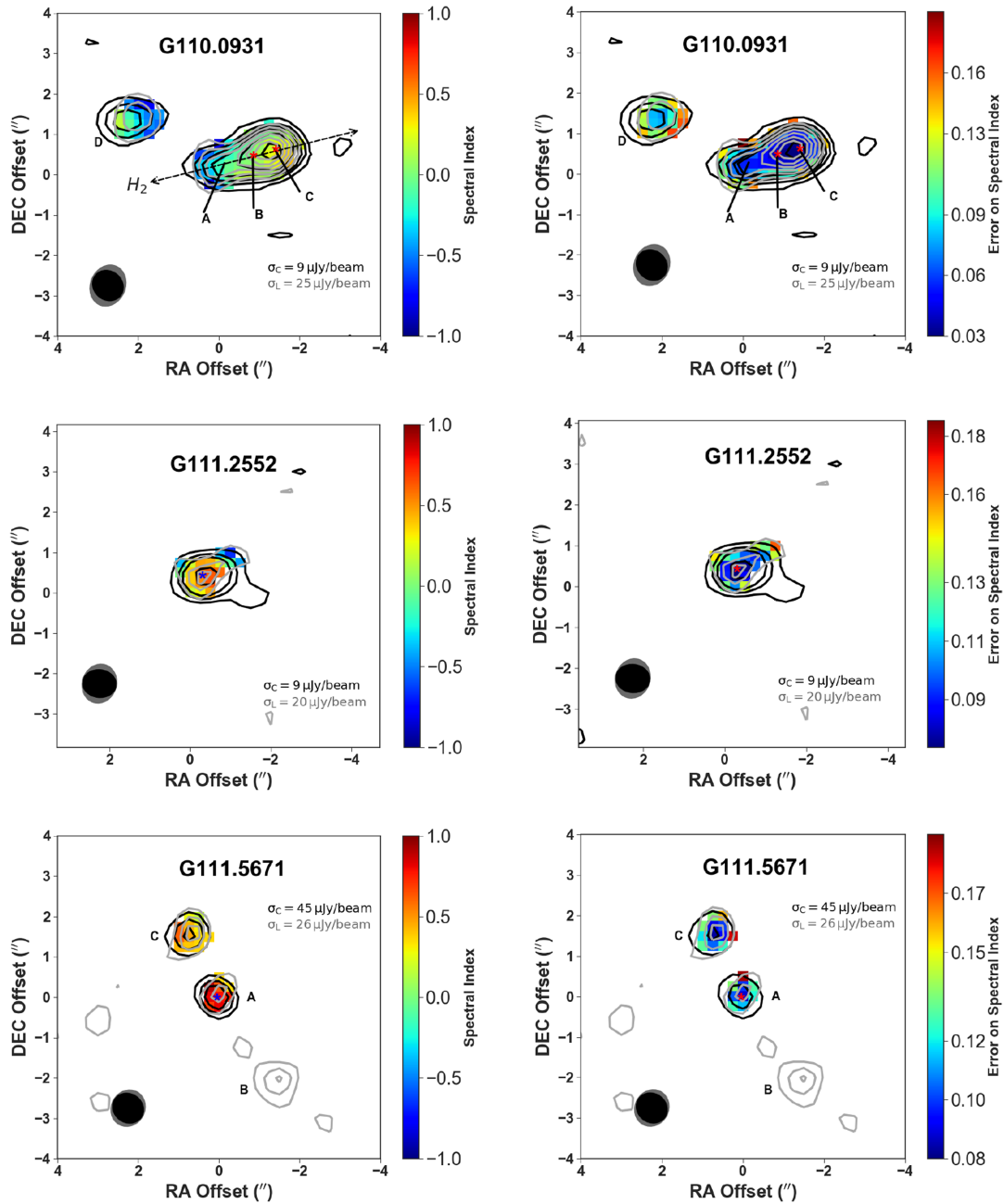
Figure 3. - *continued.*

magnetic fields. It is, however, not clear if the magnetic fields are generated in the surrounding interstellar medium or by the protostars themselves. The non-thermal emission, present on an object's spectral index map, is mainly seen further away from the central source, confirming that the central sources are thermal while the jet lobes are not. Detailed comments on each object are given in the appendix.

5.3 Nature of the cores and their radio luminosity at *L* band

The nature of the cores and their *L*-band emission were examined further by exploring the distribution of the cores on a bolometric-colour plot and the relationship between bolometric- and radio-luminosities at *L* band.

5.3.1 Relationship between infrared colour and bolometric luminosity

The infrared colour of young stellar objects is likely to be related to their evolution, as they become bluer with age. A plot of mid-infrared colour versus bolometric luminosity of the sample, shown in Fig. 4, suggests that MYSOs of higher bolometric luminosities are more likely to have lobes compared to their lower luminosity counterparts, especially at lower values of $\frac{F_{21\,\mu m}}{F_{8\,\mu m}}$. Whether this property of the jets is related to their evolution or driving power is not clear. However, the radio luminosity of a jet is correlated with its bolometric luminosity and force (Anglada, Rodríguez & Carrasco-Gonzalez 2015), implying that sources with higher bolometric luminosity are likely to have more powerful lobes that are easily detectable in the radio compared to sources of lower luminosity.
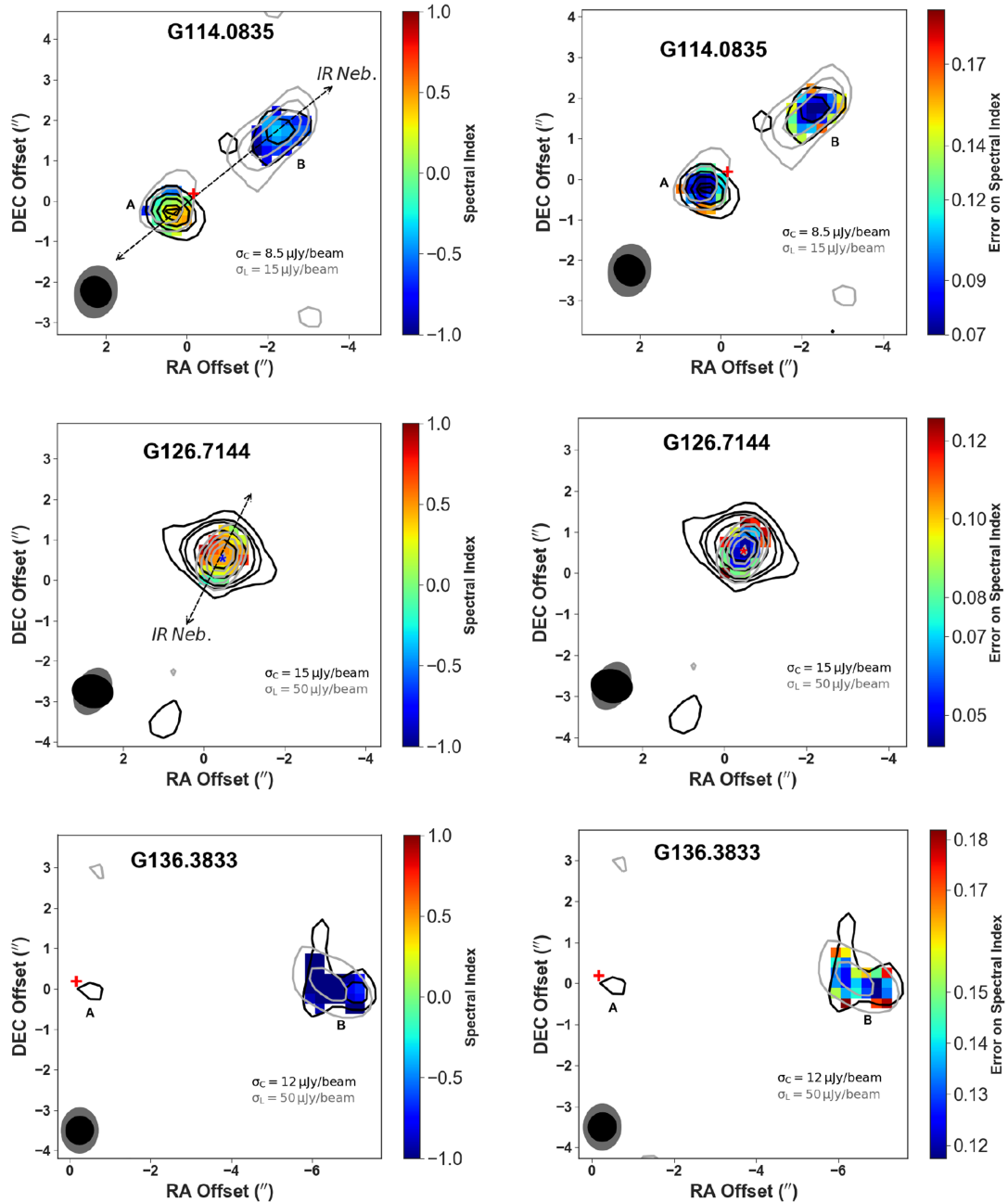
Figure 3. *- continued.*

5.3.2 Relationship between L-band radio luminosity and bolometric luminosity

The radio luminosities of thermal radio jets show a correlation with bolometric luminosities. Different studies find the slope of the correlation to lie in the range of 0.6–0.9 in a log–log plot. Cabrit & Bertout (1992) and Anglada (1995) estimated it as 0.8 and 0.6, respectively. Recently, Shirley et al. (2007) found the slope to be ∼0.9 and 0.7 at 5 and 8.3 GHz, respectively, in low-mass stars. At L band, we find a slope of 0.64 ± 0.03. This slope is for all the objects on the plot shown in Fig. 5, consisting of cores of L-band sources and thermal radio jets taken from the literature. Fluxes of the sources from the literature were scaled to L-band frequency using a spectral index of 0.6. High-mass sources in the

plot show a slope of ∼0.57 ± 0.15, consistent with the lower end of the previous estimates, i.e. ∼ 0.6–0.9. In spite of the evidence of non-thermal emission at L band, the cores are largely thermal, manifesting the properties of free–free emitters and showing no significant effect on the slope. The lower slope of high-mass sources may be due to a smaller range of luminosity and uncertainties in their distances and fluxes. Clearly, the slopes are comparable to Anglada et al. (2018) who derived an empirical equation relating the two quantities at 8.3 GHz for objects of bolometric luminosities ∼1 L$_\odot$ ≤ $L_{\rm bol}$ ≤ 10^6 L$_\odot$ (see equation 1):

$$\left(\frac{S_\nu d^2}{\mathrm{mJy\,kpc^2}} \right) = 10^{-1.90 \pm 0.07} \left(\frac{L_{\rm bol}}{\mathrm{L_\odot}} \right)^{0.59 \pm 0.03}. \tag{1}$$
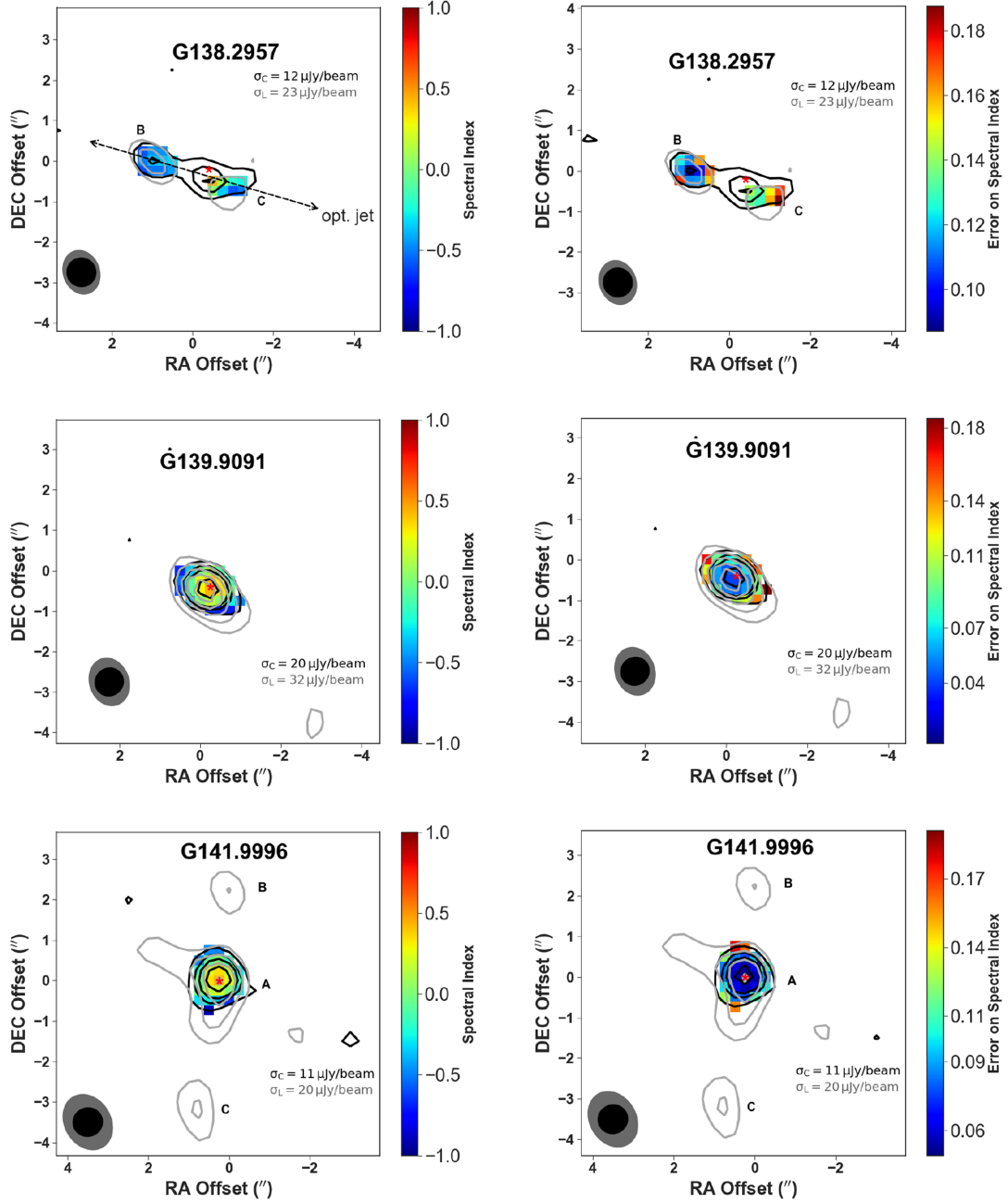
Figure 3. - *continued.*

The slopes, as seen in Fig. 5, demonstrate the similarity between low- and high-mass protstellar jets, owing to the comparable radio-bolometric luminosity correlations, implying that they have a common ionization, and perhaps driving mechanism.

5.4 Derived properties of the radio jets

Quantities such as the jets' mass-loss rates, injection radius and opening angles can be estimated from the fluxes and angular sizes of their cores. Fluxes and angular sizes of the cores at *L* band, together with their spectral indices, were used to calculate some of these properties in accordance with the Reynolds (1986) model.

5.4.1 Mass-loss rate

Reynolds (1986) modelled free–free emission from an ionized jet. The model can be used to calculate the mass-loss rate through the jet if its ionization fraction, electron temperature, terminal velocity and an inclination angle to the line of sight are known. The model estimates the mass-loss rate through a conical jet of pure hydrogen, electron temperature $T_e = 10^4$ K, and inclination angle $i = 90°$, in units of $10^{-6}\,\mathrm{M_\odot\,yr^{-1}}$, to be

$$\dot{M}_{-6} = 0.938 v_t x_o^{-1} \left(\frac{\mu}{m_p}\right) S_{mJy}^{0.75} \upsilon_o^{-0.75\alpha} d_{kpc}^{1.5} \upsilon_m^{0.75\alpha-0.45} \theta_o^{0.75} F^{-0.75},$$

(2)
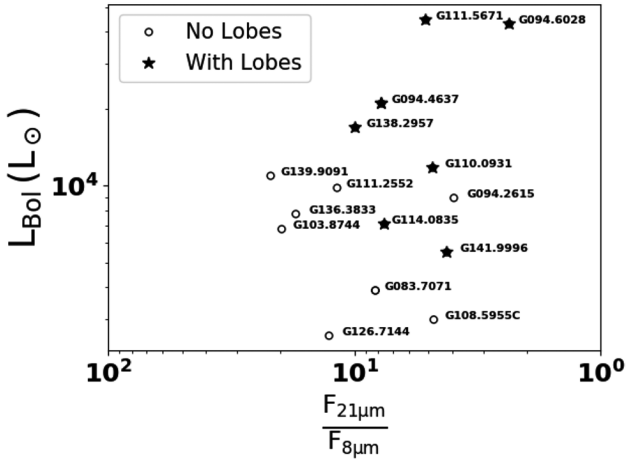
Figure 4. An illustration showing how mid-IR colour of MYSOs varies with bolometric luminosity.

where α, μ, m_p, v_t, x_o, S_{mJy}, v_o, v_m, d_{kpc}, and θ_o are the derived spectral index, mean particle mass per hydrogen atom, proton mass, terminal velocity of the jet in 10^3 kms^{-1}, ionization fraction, observed flux density in mJy, frequency of observation (here L band) in units of 10 GHz, turnover frequency in units of 10 GHz, object's distance in kpc and the opening angle (in radians given as $\theta_o = 2 \tan^{-1}(\frac{\theta_{min}}{\theta_{maj}})$; Eisloffel et al. 2000) respectively. F is a quantity that depends on the opacity and spectral index of a jet given as (Reynolds 1986)

$$F \equiv F(q_\tau, \alpha) = \frac{2.1^2}{q_\tau(\alpha - 2)(\alpha + 0.1)}, \qquad (3)$$

where q_τ is a quantity that describes how opacity varies along the jet. F was calculated using the parameters of a standard spherical jet model if the spectral index of a source lies in the range $0.4 \leq \alpha \leq 0.8$ and standard collimated model if $0 < \alpha < 0.4$. q_τ was taken to be -3 if $0.4 \leq \alpha \leq 0.8$ and -2 for $0 < \alpha < 0.4$. The ionization fraction of MYSO jets is determined by collisions within the jets (Hartigan, Morse & Raymond 1994; Bacciotti & Eislöffel 1999; Bacciotti 2002) and perhaps ionizing radiation from the central source. Typical values of jet ionization fraction x_o are $\sim$0.02–0.4 (Bacciotti & Eislöffel 1999; Bacciotti 2002), a quantity that varies along a jet in accordance with recombination models. The maximum value of ionization fraction in the literature ($x_o = 0.4$) was used in the calculation of mass-loss rate in this work as all the YSOs considered here are massive and are expected to have more powerful jets that are better collisional ionizers. Terminal velocity of jet materials (or simply jet velocity) was estimated from its range i.e. $\sim$270 km s^{-1} in low-mass stars to $\sim$1000 km s^{-1} in high-mass stars (Anglada et al. 2015). The average velocity of optical jets is $\sim$750 km s^{-1} (Mundt & Ray 1994), a value comparable to Jiménez-Serra et al. (2011) and Martí et al. (1998) estimates of $\sim$500 km s^{-1} in Cepheus A HW2 and HH 80-81, respectively. Whereas the average velocity in optical jets is $\sim$750 km s^{-1}, a value of $v_t = 500$ km s^{-1}, estimated via proper motion of a radio jet (Martí et al. 1998) was adopted as a reasonable approximation of the sample's jets' terminal velocity, in calculating the mass-loss rate. A turnover frequency of 50 GHz was assumed as the value is generally expected to be higher than 40 GHz (Anglada et al. 2018). Finally, a semi-opening angle of $31° \pm 3$, the average semi-opening angle for nine sources whose angles were calculated directly, was adopted for sources whose angles could not be estimated from $\theta_o = 2 \tan^{-1}(\frac{\theta_{min}}{\theta_{maj}})$. The range of the calculated semi-opening angles, 25–35°, is comparable to the estimate by Moscadelli et al. (2016) i.e. $20° \pm 5°$.

Figure 5. Relationship between *L*-band radio luminosity and bolometric luminosity for thermal radio sources. The asterisks represents the MYSOs under study while the empty circles and triangles represent the cores of low- and high-mass jets from Anglada (1995) and Anglada et al. (2018), respectively.
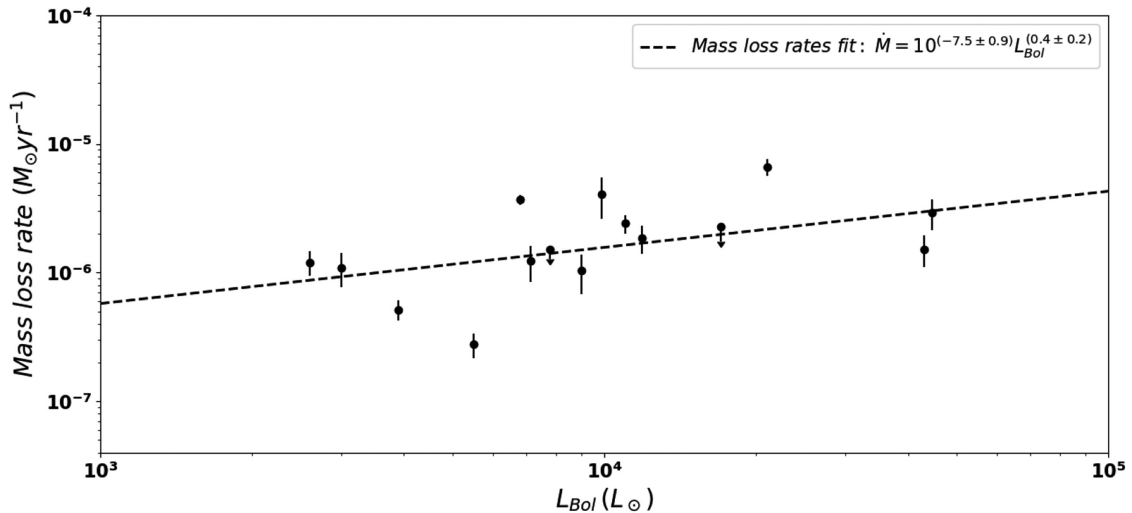
Figure 6. A plot showing how mass-loss rates of the sources vary with their bolometric luminosity.

The sample's mass-loss rates $\dot{M}$ lie in the range $\sim 2.8 \pm 0.6 \times 10^{-7}$ to $6.6 \pm 0.9 \times 10^{-6}\,\mathrm{M_\odot\,yr^{-1}}$ (see Fig. 6), typical of rates from MYSO (Poetzel, Mundt & Ray 1993; Mundt & Ray 1994; Purser et al. 2016) and $\sim 10^2$–10^3 higher than low-mass counterparts. Mass-loss rates of the MYSOs were found to be related to their bolometric luminosity by the equation $\dot{M} \simeq 10^{-7.5 \pm 0.9} L_{\mathrm{bol}}^{0.4 \pm 0.2}$. Although low-mass YSOs are expected to have lower mass-loss rates ($\sim 10^{-10}$–$10^{-8}\,\mathrm{M_\odot\,yr^{-1}}$; Mundt & Ray 1994; Hartigan, Edwards & Ghandour 1995a; Konigl & Pudritz 2000), some of them have rates that are comparable with high-mass ones, in effect implying that distinguishing such jets from high-mass ones (Ceccarelli et al. 1997) is not straightforward.

5.4.2 Accretion rate

Stellar jet outflows are considered to be closely related to accretion inflows (Pudritz et al. 2007), therefore it is reasonable to estimate accretion rates of YSOs from their mass-loss rates. Hartigan, Edwards & Ghandour (1995b) empirically established a correlation between accretion and mass-loss rates of low mass stars where they demonstrated that $0.00008 \leq \frac{\dot{M}}{\dot{M}_{acc}} \leq 0.4$ with an average value of 0.01. Matt & Pudritz (2005) also modelled MHD jets and found that the stellar angular momentum problem in YSOs can only be solved if jet outflow rates are ~ 10 per cent of accretion rates although magnetic field strength can influence the ratio. This value lies within Hartigan et al. (1995b)'s range, albeit a factor of 10 above the average.

The average value of $\frac{\dot{M}}{\dot{M}_{acc}} \sim 0.01$ in Hartigan et al. (1995b)'s work was therefore used in estimating accretion rates resulting in $\dot{M}_{acc} \sim 10^{-4.6 \pm 0.3}$–$10^{-3.2 \pm 0.2}\,\mathrm{M_\odot\,yr^{-1}}$ which is consistent with high rates theoretically expected from the sources i.e. $\sim 10^{-4}$–$10^{-3}\,\mathrm{M_\odot\,yr^{-1}}$ (McKee & Tan 2002). The accretion rate of one of the sources, G094.6028, $1.5 \pm 0.4 \times 10^{-4}\,\mathrm{M_\odot\,yr^{-1}}$ was found to be comparable to $\sim 1.2 \pm 0.06 \times 10^{-4}\,\mathrm{M_\odot\,yr^{-1}}$ (Pomohaci et al. 2017), derived using hydrogen Bracket gamma spectral lines.

6 CONCLUSIONS

We studied a sample of 15 MSYOs, at least 40 per cent of which show evidence of non-thermal emission. Six of the sources,

G094.6028, G103.8744, G111.5671, G114.0835, G138.2957 and G141.9996, manifest non-thermal radio lobes, similar to those seen in HH objects. The study, therefore, suggests that massive stars form via accretion discs in a manner similar to low-mass stars but with high accretion rates.

All the MYSOs have thermal central sources that are considered the drivers of the jets. The average spectral index of the thermal sources is $\sim 0.42 \pm 0.27$, clearly similar to the theoretical 0.6, expected from ionized winds. They drive the jets at a rate higher than low-mass counterparts with mass-loss rates $\sim 3 \times 10^{-7}$ to $7 \times 10^{-6}\,\mathrm{M_\odot\,yr^{-1}}$.

Clearly, lobes of some MYSO jets confirm the presence of synchrotron emission, implying the presence of magnetic fields and charged particles at relativistic velocities. This finding suggests that magnetic fields play a significant role in the jets, perhaps in driving them from the core (Blandford & Payne 1982; Shu et al. 1994). However, a thermal jet can also interact with ambient magnetic field producing non-thermal emission. A study of 46 young MYSOs by Purser et al. (2016) also found that about 50 per cent of the sample may be associated with non-thermal lobes, again emphasizing the significance of magnetic fields in jets of massive protostars.

It was also found that sources of higher bolometric luminosity are more likely to have lobes compared to lower luminosity counterparts and that some of them may be variable.

REFERENCES

Anglada G., 1995, in Lizano S., Torrelles J. M., eds, Revista Mexicana de Astronomia y Astrofisica Conference Series, Vol. 1, Instituto de Astronomia , Mexico. p. 67

Anglada G., Rodríguez L. F., Carrasco-Gonzalez C., 2015, Proc. Sci., 215, 121

Anglada G., Rodríguez L. F., Carrasco-González C., 2018, A&AR, 26, 3

Bacciotti F., 2002, in Henney W. J., Steffen W., Binette L., Raga A., eds, Revista Mexicana de Astronomia y Astrofisica Conference Series, Vol. 13, Instituto de Astronomia, Mexico, p. 8

Bacciotti F., Eislöffel J., 1999, A&A, 342, 717

Banerjee R., Pudritz R. E., 2007, ApJ, 660, 479

Bell A. R., 1978, MNRAS, 182, 147

Blandford R., Eichler D., 1987, Phys. Rep., 154, 1

Blandford R. D., Payne D. G., 1982, MNRAS, 199, 883

BriggsD.S., 1995, PhD thesis, New Mexico Institute of Mining and Technology

Brooks K. J., Garay G., Mardones D., Bronfman L., 2003, ApJ, 594, L131

Cabrit S., Bertout C., 1992, A&A, 261, 274

Caratti o Garatti A. et al., 2016, A&A, 589, L4

Carral P., Kurtz S., Rodríguez L. F., Martí J., Lizano S., Osorio M., 1999, RMxAA, 35, 97

Carrasco-González C. et al., 2015, Science, 348, 114

Carrasco-González C., Rodríguez L. F., Anglada G., Martí J., Torrelles J. M., Osorio M., 2010, Science, 330, 1209

Carrasco-González C., Rodríguez L. F., Anglada G., Martí J., Torrelles J. M., Osorio M., 2013, in European Physical Journal Web of Conferences, Vol. 61, European Physical Journal Web of Conferences, EPD Sciences, London, p. 03003

Casali M. et al., 2007, A&A, 467, 777

Ceccarelli C., Haas M. R., Hollenbach D. J., Rudolph A. L., 1997, ApJ, 476, 771

Cesaroni R. et al., 2018, A&A, 612, A103

Clarke A. J. et al., 2006, A&A, 457, 183

Cohen M., 1977, ApJ, 215, 533

Curiel S. et al., 2006, ApJ, 638, 878

Davis C. J., Moriarty-Schieven G., Eislöffel J., Hoare M. G., Ray T. P., 1998, AJ, 115, 1118

De Buizer J. M., Radomski J. T., Telesco C. M., Pi na R. K., 2005, ApJS, 156, 179

de Gouveia Dal Pino E. M., 2005, Adv. Space Res., 35, 908

de Wit W. J. et al., 2009, A&A, 494, 157

DeSouza A. L., Basu S., 2015, MNRAS, 450, 295

Di Francesco J., Evans N. J., II, Harvey P. M., Mundy L. G., Guilloteau S., Chandler C. J., 1997, ApJ, 482, 433

Dobashi K., Uehara H., 2001, PASJ, 53, 799

Eisloffel J., Mundt R., Ray T. P., Rodriguez L. F., 2000, Protostars and Planets IV, University of Arizona Press, Mannings, Tucson, AZ, p. 815

Eisner J. A. et al., 2015, MNRAS, 447, 202

Fontani F., Cesaroni R., Testi L., Molinari S., Zhang Q., Brand J., Walmsley C. M., 2004, A&A, 424, 179

Gomez J. F., Torrelles J. M., Estalella R., Anglada G., Verdes-Montenegro L., Ho P. T. P., 1992, ApJ, 397, 492

Guzmán A. E., Garay G., Brooks K. J., 2010, ApJ, 725, 734

Guzmán A. E., Garay G., Brooks K. J., Voronkov M. A., 2012, ApJ, 753, 51

Hamann F., Persson S. E., 1989, ApJ, 339, 1078

Hartigan P., Morse J. A., Raymond J., 1994, ApJ, 436, 125

Hartigan P., Edwards S., Ghandour L., 1995a, in Pena M., Kurtz S., eds, Revista Mexicana de Astronomia y Astrofisica, vol. 27, Vol. 3, Revista Mexicana de Astronomia y Astrofisica Conference Series, Instituto de Astronomia, Mexico, p. 93

Hartigan P., Edwards S., Ghandour L., 1995b, ApJ, 452, 736

Hewett P. C., Warren S. J., Leggett S. K., Hodgkin S. T., 2006, MNRAS, 367, 454

Hoare M. G., 2006, ApJ, 649, 856

Jiang Z., Yao Y., Yang J., Ishii M., Nagata T., Nakaya H., Sato S., 2001, AJ, 122, 313

Jiménez-Serra I., Martín-Pintado J., Báez-Rubio A., Patel N., Thum C., 2011, ApJ, 732, L27

Konigl A., Pudritz R. E., 2000, Protostars and Planets IV, University of Arizona Press, Mannings, Tucson, AZ, p. 759

Kraus S. et al., 2010, Nature, 466, 339

Kuiper R., Klahr H., Beuther H., Henning T., 2014, in Stamatellos D., Goodwin S., Ward-Thompson D., eds, Astrophysics and Space Science

Proceedings, Vol. 36, The Labyrinth of Star Formation, Springer international publishing, Switzerland, p. 379

Kuiper R., Yorke H. W., Turner N. J., 2015, ApJ, 800, 86

Kumar Dewangan L., Anandarao B. G., 2010, MNRAS, 402, 2583

Kumar M. S. N., Bachiller R., Davis C. J., 2002, ApJ, 576, 313

Kurtz S., Churchwell E., Wood D. O. S., 1994, ApJS, 91, 659

Lawrence A. et al., 2007, MNRAS, 379, 1599

Levshakov S. A., Henkel C., Reimers D., Wang M., Mao R., Wang H., Xu Y., 2013, A&A, 553, A58

López-Cámara D., Raga A. C., 2010, ApJ, 723, 449

Lu X., Zhang Q., Liu H. B., Wang J., Gu Q., 2014, ApJ, 790, 84

Lucas P. W. et al., 2008, MNRAS, 391, 136

Lumsden S. L. et al., 2013, ApJS, 208, 11

Manjarrez G., Gómez J. F., de Gregorio-Monsalvo I., 2012, MNRAS, 419, 3338

Martí J., Rodríguez L. F., Reipurth B., 1998, ApJ, 502, 337

Matt S., Pudritz R. E., 2005, MNRAS, 356, 167

McKee C. F., Tan J. C., 2002, Nature, 416, 59

McMullin J. P., Waters B., Schiebel D., Young W., Golap K., 2007, in Shaw R. A., Hill F., Bell D. J., eds, ASP Conf. Ser. Vol. 376, Astronomical Data Analysis Software and Systems XVI. Astron. Soc. Pac., San Francisco, p. 127

Meyer D. M.-A., Vorobyov E. I., Kuiper R., Kley W., 2017, MNRAS, 464, L90

Mitchell G. F., Hasegawa T. I., 1991, ApJ, 371, L33

Mitchell G. F., Lee S. W., Maillard J.-P., Matthews H., Hasegawa T. I., Harris A. I., 1995, ApJ, 438, 794

Moscadelli L. et al., 2016, A&A, 585, A71

Mundt R., Ray T. P., 1994, in The P. S., Perez M. R., van den Heuvel E. P. J., eds, ASP Conf. Ser. Vol. 62, The Nature and Evolutionary Status of Herbig Ae/Be Stars. Astron. Soc. Pac., San Francisco, p. 237

Navarete F., Damineli A., Barbosa C. L., Blum R. D., 2015, MNRAS, 450, 4364

Poetzel R., Mundt R., Ray T. P., 1993, in Errico L., Vittone A. A., eds, Astrophysics and Space Science Library, Vol. 186, Stellar Jets and Bipolar Outflows. p. 231

Pomohaci R., Oudmaijer R. D., Lumsden S. L., Hoare M. G., Mendigutía I., 2017, MNRAS, 472, 3624

Pudritz R. E., Banerjee R., 2005, in Cesaroni R., Felli M., Churchwell E., Walmsley M., eds, Proc. IAU Symp. 227, Massive Star Birth: A Crossroads of Astrophysics, Cambridge University Press, Cambridge. p. 163

Pudritz R. E., Norman C. A., 1986, ApJ, 301, 571

Pudritz R. E., Ouyed R., Fendt C., Brandenburg A., 2007, Protostars and Planets V, University of Arizona Press, Tucson, AZ. p. 277

Purser S. J. D. et al., 2016, MNRAS, 460, 1039

Purser S. J. D., 2017, PhD thesis, Univ. Leeds

Raga A. C., Kofman L., Falle S. A. E. G., 1993, in Errico L., Vittone A. A., eds, Astrophysics and Space Science Library, Vol. 186, Stellar Jets and Bipolar Outflows, Springer, Dordrecht. p. 301

Ray T. P., Poetzel R., Solf J., Mundt R., 1990, ApJ, 357, L45

Reipurth B., Bally J., 2001, ARA&A, 39, 403

Rengarajan T. N., Ho P. T. P., 1996, ApJ, 465, 363

Reynolds S. P., 1986, ApJ, 304, 713

Rodríguez T., Trinidad M. A., Migenes V., 2012, ApJ, 755, 100

Rodríguez-Kamenetzky A. et al., 2016, ApJ, 818, 27

Rodríguez-Kamenetzky A. et al., 2017, ApJ, 851, 16

Rosero V. et al., 2016, ApJS, 227, 25

Rubini F., Lorusso S., Del Zanna L., Bacciotti F., 2007, A&A, 472, 855

Sánchez-Monge Á., Palau A., Estalella R., Beltrán M. T., Girart J. M., 2008, A&A, 485, 497

Sandell G., Goss W. M., Wright M., 2005, ApJ, 621, 839

Sanna A. et al., 2019, A&A, 623, A77

Schreyer K., Henning T., van der Tak F. F. S., Boonman A. M. S., van Dishoeck E. F., 2002, A&A, 394, 561

Schulz A., Black J. H., Lada C. J., Ulich B. L., Martin R. N., Snell R. L., Erickson N. J., 1989, ApJ, 341, 288

Shirley Y. L., Claussen M. J., Bourke T. L., Young C. H., Blake G. A., 2007, ApJ, 667, 329

Shu F. H., Najita J., Ruden S. P., Lizano S., 1994, ApJ, 429, 797

Skrutskie M. F. et al., 2006, AJ, 131, 1163

Smith H. A., Fischer J., 1992, ApJ, 398, L99

Tofani G., Felli M., Taylor G. B., Hunter T. R., 1995, A&AS, 112, 299

Trinidad M. A., Curiel S., Torrelles J. M., Rodríguez L. F., Migenes V., Patel N., 2006, AJ, 132, 1918

Urquhart J. S. et al., 2011, MNRAS, 418, 1689

Vaidya B., Fendt C., Beuther H., 2009, ApJ, 702, 567

van der Tak F. F. S., Menten K. M., 2005, A&A, 437, 947

Varricatt W. P., Davis C. J., Ramsay S., Todd S. P., 2010, MNRAS, 404, 661

Velusamy T., Langer W. D., Marsh K. A., 2007, ApJ, 668, L159

Vig S., Veena V. S., Mandal S., Tej A., Ghosh S. K., 2018, MNRAS, 474, 3808

Wang Y. et al., 2016, A&A, 587, A69

Wang K.-S., van der Tak F. F. S., Hogerheijde M. R., 2012, A&A, 543, A22

Wolf-Chase G., Arvidsson K., Smutko M., 2017, ApJ, 844, 38

Wouterloot J. G. A., Henkel C., Walmsley C. M., 1989, A&A, 215, 131

Wu Y.-W., Xu Y., Yang J., Li J.-J., 2009, Res. Astron. Astrophys., 9, 1343

Xu J.-L., Wang J.-J., 2010, Res. Astron. Astrophys., 10, 151

APPENDIX: DISCUSSION OF INDIVIDUAL OBJECTS

A1 G083.7071

Two sources A and B were detected in the field (see Fig. A1). Source A whose spectral index $\alpha = 0.44 \pm 0.10$ is the MYSO. The *L*-band emission of A is elongated, perhaps signifying presence of a jet. Apart from the MYSO, source B, located $\sim$3.5 arcsec to the SW of A was also detected in the field. This source was detected in UKIDSS's IR *K* band just like A but not at *Q* band where the rms noise $\sim$29 μJy beam^{-1}. It is a thermal radio source of *L*–*C* spectral index $\alpha_{LC} \sim 0.60 \pm 0.13$, perhaps another MYSO.
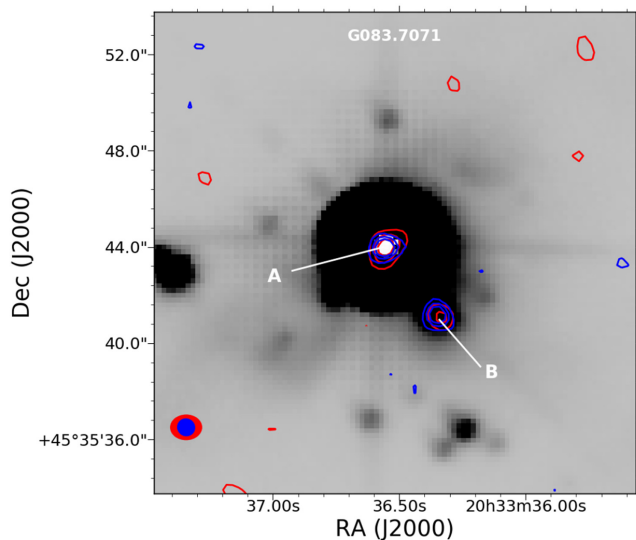

Figure A1. UKIDSS *K*-band IR image of the field with *L*- and *C*-band contours shown in red and blue lines, respectively.
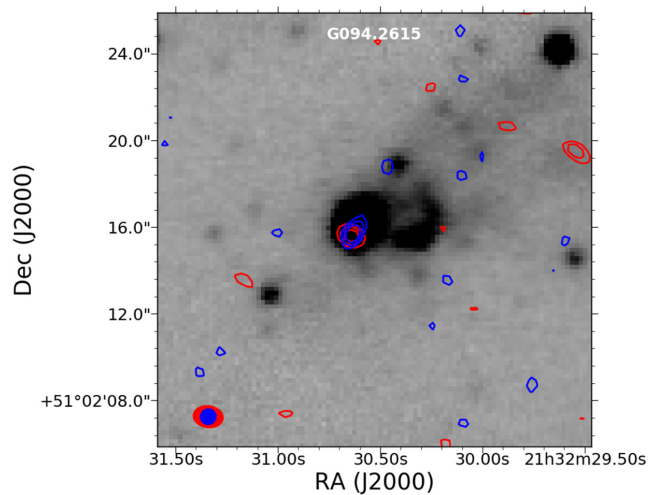
Figure A2. G094.2615 UKIDSS *K*-band map with *L*- and *C*-band contours shown in red and blue lines, respectively.

A2 G094.2615

G094.2615 is made up of two sources, A1 and A2 (Purser et al., in preparation), clearly seen in the *C*-band map of high resolution (see Fig. 1). Its *L*–*C* band spectral index is lower than that of *C*–*Q* band that could be due to non-thermal contribution at *L* eventhough the overall spectral index shows that it is thermal, i.e. $\alpha_v = 0.23 \pm 0.18$. A1 was detected at both *C* and *Q* bands, giving it a *C*–*Q* spectral index of 0.47 ± 0.24, consistent with the MYSO core. UKIDSS map of the field (Fig. A2) shows emission that is largely aligned in a SE-NW direction similar to that of *C* band. The UKIDSS emission, 2.12 μm H_2 line emission (Varricatt et al. 2010; Wolf-Chase et al. 2017) and CO molecular outflow (Fontani et al. 2004) all points to a source that drives a jet in a SE-NW direction. There is also an NIR emission to the west of the MYSO but its source is unclear.

A3 G094.4637

Two sources, G094.4637(A+B+C+D) and a lobe (source E), of spectral indices 0.53 ± 0.09 and 0.21 ± 0.45, respectively, were detected at *L* band. The spectral index of G094.4637(A+B+C+D) suggests that it is thermal, but one of its component D show non-thermal property (Fig. 3). Lobe E is aligned with components A, B, and D in such a way that they exhibit a central thermal core and associated jet lobes. Its *C*- and *L*-band emissions are slightly offset in a NE–SW direction, similar to that of the outflow, consequently giving it a non-thermal property towards the SW where *L*-band emission is stronger and a thermal characteristic towards the NE. The displacement of its *L*-band emission is consistent with that of a jet originating from A and directed towards E.

Of the four sources, only A appears to be the core given its proximity to the IR source. Again, it is the only source in the group that was detected at *Q* band (Purser 2017) where it splits into two thermal sources A and A2 of *C*–*Q* band spectral indices 0.39 ± 0.12 and $>1.47 \pm 0.17$, suggesting that it is a binary and A or A2 drives the jet. The morphology of *L*-band emission as well as the alignment of the sources in *C*-band also suggests presence of a jet. The results of Smith & Fischer (1992) and Navarete et al. (2015) indicate the presence of multiple jets. Navarete et al. (2015), for example, detected a monopolar and two bipolar outflows in the field. Two of their outflows, 2a and 3a, have position angles that are
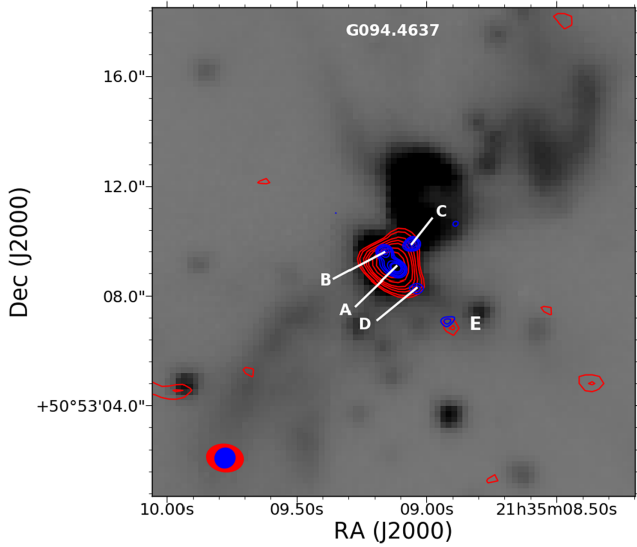
Figure A3. G094.4637 UIST map together with *L*- and *C*-band contours shown in red and blue, respectively. Both *L*- and *C*-band contours start from 3σ and increase in steps of 2σ and 4σ, respectively.
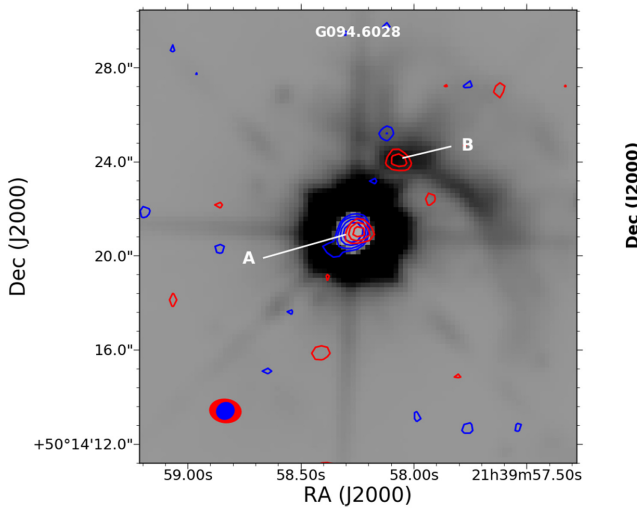

Figure A4. G094.6028 UKIDSS *K*-band map with *L* (3,4,5 σ)-band and *C*(3,5, 9,15 σ)-band contours shown in red and blue continuous lines, respectively.

comparable to the position angles of D and C from the location of the IR source i.e ∼ 210° and 330°, respectively. Despite the evidence of multiple outflows in the field, the driving sources are not clear from both *L*- and *C*-band emissions. Source C, detected at *Q* band (Purser 2017), may also be a thermal core. Its *C*–*Q* band spectral index is $\alpha_{CQ} \sim 0.86 \pm 0.05$. The source is located at a position angle of ∼−30° from A and is aligned with the main *K*-band NIR emission (Fig. A3), hence is a potential thermal core. A 12.5 μm image of the field also display two sources,[3] possibly A and C, aligned in a SE-NW direction, confirming that there are two cores.

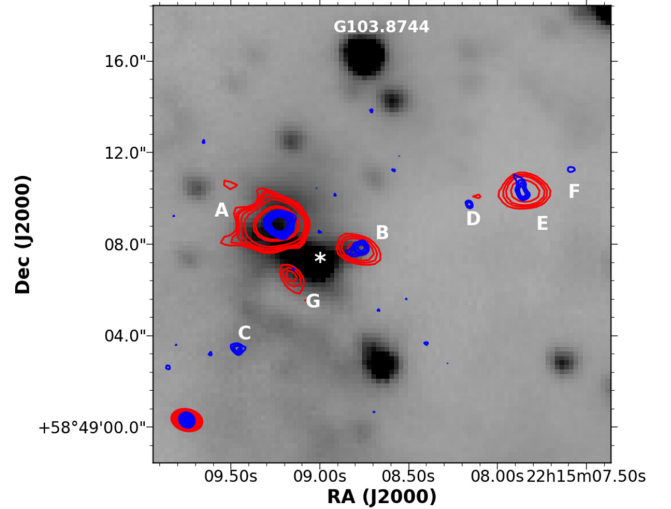[3]http://rms.leeds.ac.uk/cgibin/public/RMS_DATABASE.cgi

Figure A5. UKIDSS *K*-band image of G103.8744 field with *L*- and *C*-band contours shown in red and blue lines, respectively. The contour levels both start at 3σ. *C*-band ones increase in steps of 4σ, while *L* band in steps of 2σ.

A4 G094.6028

G094.6028, also known as V645 Cyg, has a thermal radio core of spectral index 0.44 ± 0.15. The source, named A (see Fig. A4), is a known variable protostar of spectral type ∼O7-O9 (Cohen 1977). Earlier observation of the source by Di Francesco et al. (1997) at 8.3 GHz registered a higher flux, perhaps confirming its variability (Clarke et al. 2006). Apart from the MYSO, a nearby source, B, of flux density 0.07 ± 0.02 mJy was also detected ∼4 arcsec away to the NW at *L* band but not *C* band. It appears to be a non-thermal lobe of spectral index < -0.42. The MYSO is known to emit Brγ, accrete material, drive bipolar CO outflow and harbour a circumstellar disc (Hamann & Persson 1989; Schulz et al. 1989; Clarke et al. 2006; Eisner et al. 2015).

A5 G103.8744

G103.8744 is associated with the IRAS source 22134+5834. It has five radio sources in its field, three of which are within a radius of ∼3 arcsec from the location of the IR source (white asterisk in Fig. A5). Both A and B are thermal and are close to the location of the MYSO but their spectra suggest that they are H ɪɪ regions (see Fig. A6; spectrum of G103.8744-B). Indeed, A is a known ultra-compact H ɪɪ region (Wang et al. 2016) whose turnover frequency seems to lie between 5 and 8.3 GHz (see Fig. 2). B has a fainter but compact IR counterpart suggesting that it is a source, perhaps a low-mass YSO or an obscured massive protostar. Source G, on the other hand, was not detected at *C* band where rms noise is ∼15 μJy beam^{-1} implying that it is a non-thermal radio source whose spectral index is < -0.44.

Seeing that B has an IR counterpart and sources B, D, E, F, and G are all aligned in a SE-NW direction, reminiscent of jet lobes, B could be the jet driver. Wang et al. (2016) imaged the source at radio frequencies but could not separate the MYSO from the H ɪɪ region. They estimated a combined flux for the sources as 2.1 ± 0.2, 3.5 ± 0.11, and 2.9 ± 0.70 mJy at 1.3, 6.0, and 20 cm respectively. These fluxes were also used in generating the spectrum of source A, as it is the dominant emitter in the field. A map of H_2 emission line at 2.12 μm does not reveal any clear evidence of shocks or photo-
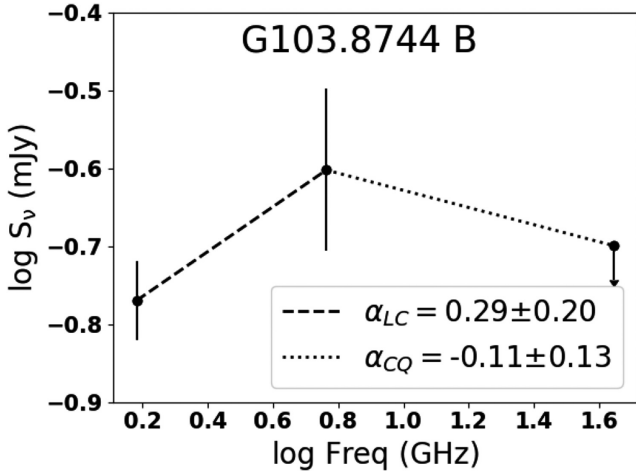
Figure A6. Spectrum of G103.8744-B.

dissociation locations (Kumar, Bachiller & Davis 2002); however, its $C^{18}O$ $(J = 1 - 0)$ map displays an outflow (Dobashi & Uehara 2001) in a direction similar to that of the IR emission i.e. a position angle PA $\sim 45°$.

A6 G108.5955C

L- and *C*-band emission of G108.5955C show different morphologies. Its *L–C* band spectral index $\alpha_{LC} = 0.20 \pm 0.16$ shows that it is thermal but the spectral index map displays evidence of non-thermal emission on the eastern part. Both Wu et al. (2009) and Xu & Wang (2010) detected molecular outflows in the field; however, 2.12 μm H_2 line map (Wolf-Chase et al. 2017) does not show any evidence of knots which may be associated with the source.

A7 G110.0931

G110.0931's field contains two *L*-band sources, the MYSO and source D (see Fig. 1), whose *L–C* band spectral indices are 0.36 ± 0.14 and -0.08 ± 0.15, respectively. The MYSO encompasses three sources: A, B, and C of spectral indices $\alpha_\nu = -0.14 \pm 1.49$, 0.33 ± 0.14, and -0.11 ± 0.07, respectively (Rodríguez et al. 2012; Purser 2017).

Unlike B and C, A was not detected at *Q* band (Purser 2017) consequently giving G110.0931 overall an H II region-like spectrum. The detection of sources B and C at *Q* band suggests that they could be cores, though we note that only B is detected by NOEMA[4] at 1.3 mm (Bosco et al., in preparation), whereas we would expect any core at this evolutionary stage to be detectable in the mm. Overall, it seems likely therefore that B is the core and A and C are jet lobes. Source D, detected on the eastern part of G110.0931, was not detected at *Q* band where the field rms is ~ 0.044 mJy beam^{-1}, setting a limit on its spectral index as $\alpha \leq -0.12$, suggesting that it may be an optically thin H II region. This source does not show any clear association with G110.0931 that is approximately 3.3 arcsec away from it.

Navarete et al. (2015) detected a bipolar outflow that is aligned in a direction similar to that of both *L*- and *C*-band emission. 2MASS IR emission as well as the *K*-band continuum emission shown in Navarete et al. (2015) are also oriented in the same direction. Lu et al.

---

[4]NOrthern Extended Millimeter Array

(2014) detected $NH_3(1, 1)$ emission that is aligned in a direction perpendicular to the jet and passing through the location of the central source B. The orientation of $NH_3(1, 1)$ emission, which is a tracer of dense molecular gas (Levshakov et al. 2013) and that of the molecular line at 2.12 μm suggests that the source may be a disc–jet system. Finally, source C has higher radio flux compared to A, perhaps an indicator of a E-W density gradient.

A8 G111.2552

G111.2552, also known as I23139 (Trinidad et al. 2006), is a thermal radio source of spectral index $\alpha_\nu \sim 0.67 \pm 0.04$. Its *L*- and *C*-band emissions are largely aligned in a SE-NW direction (see Fig. 3). Its *Q*-band flux appears to be lower than expected (see Fig. 2) when compared to estimates from Trinidad et al. (2006), i.e. a flux density of 0.98 ± 0.24 and 0.53 ± 0.13 mJy at 23 and 8.5 GHz, respectively. Furthermore, Trinidad et al. (2006) detected a nearby source of flux density 0.22 ± 0.07 mJy, approximately 0.5 arcsec to the south, which they suppose is I23139's companion. Finally, molecular outflows (Wouterloot, Henkel & Walmsley 1989) and water maser emission (Tofani et al. 1995; Trinidad et al. 2006) detected in the field suggests presence of outflow activity (De Buizer et al. 2005).

A9 G111.5671

Three sources A, B, and C were detected in the field at *L* band. Source A, also known as NGC 7538 IRS9 (Mitchell & Hasegawa 1991), seems to be the core of G111.5671 while B and C, located ~ 2.8 and 1.7 arcsec away to the SW and NE of the core, respectively, are its lobes. *L–C* spectral indices (α_{LC}) of B and C are < -0.6 and 0.60 ± 0.21, suggesting that B is a non-thermal source while C is thermal. Also, B seems to be more diffuse, bow-shaped, and extended towards A as seen in the *C*-band image of higher resolution, suggesting that it is a bow shock.

A has a flux density of 1.00 ± 0.44 mJy, 0.76 ± 0.15 mJy (Sandell et al. 2005), and <0.51 mJy (Rengarajan & Ho 1996) at 4.86, 8.46, and 15 GHz, respectively. van der Tak & Menten (2005) used both C and A configurations of the VLA to estimate its flux density at 43 GHz, obtaining 2.9 ± 0.3 and 1.1 ± 0.3 mJy, respectively. The fluxes gives it a spectral index $\alpha = 0.84 \pm 0.09$. The three sources were previously detected by Sánchez-Monge et al. (2008) as a single source at 1.3 cm. The source, aligned in a NE–SW direction, has a spectral index of $>+0.1$. They also detected another source to the SW of A, B, and C whose spectral index is > -1.2. The orientation of the sources suggests the presence of a jet in an NE–SW direction.

Both a highly collimated HCO$^+$ outflow observed by Sandell et al. (2005) and 2.12 μm H_2 emission by Davis et al. (1998) are aligned in a NE-SW direction, similar to the alignment of the radio sources. An offshoot of the IR emission that is directed towards the south is also seen in both 2MASS and Sandell et al. (2005)'s map. This emission is in the same direction as a CO outflow (Davis et al. 1998; Sandell et al. 2005), perhaps implying presence of two outflow drivers. Furthermore, the CO $J = 2 - 1$ observed by Mitchell & Hasegawa (1991) shows a blue outflow lobe that is aligned in a NE–SW direction and a red one in the SE–NW direction.

A10 G114.0835

Two sources A and B were detected at *L* band (see Fig. 1). B is a non-thermal source of spectral index $\alpha \sim -0.42 \pm 0.19$, while A
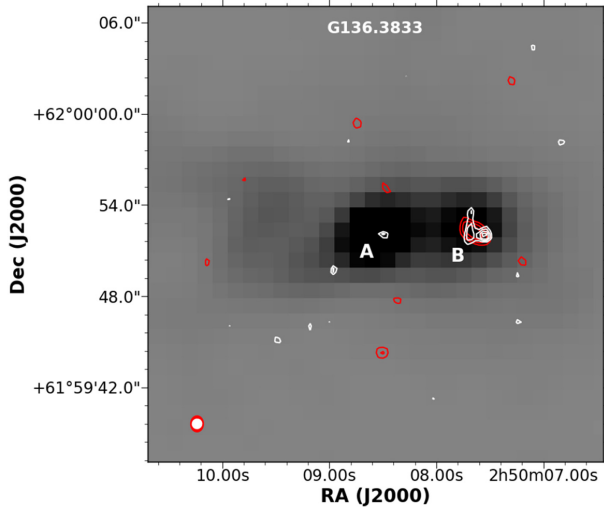
Figure A7. 2MASS *K*s band map of G136.3833 field and overplots of *L*- and *C*-band contours shown in red and white lines, respectively.

is a thermal source whose spectral index is 0.40 ± 0.20. A high-resolution image of A at C bands reveals two partially resolved sources, A1 and A2, that are oriented in a NE–SW direction. The two sources (Fig. 1) are likely to be thermal. It is not clear if A and B are associated but B is elongated in the direction of IR emission in the field (Skrutskie et al. 2006; Navarete et al. 2015), signifying the likelihood of the presence of a jet. Also, A and B are aligned in the direction of IR emission.

A11 G126.7114

G126.7114 is a thermal source of spectral index $\alpha = 0.82 \pm 0.02$ mJy. Its *L*-band and *C*-band emissions are largely aligned in a SE–NW direction. Apart from G126.7114, a weak source (4σ detection) of flux density 0.08 ± 0.02 was also detected at *C* band, approximately 4.5 arcsec away to the SE at ($\alpha = 01^h23^m33^s29$; $\delta = +061^m48^m44^s7$). NIR *K*-band emission (Jiang et al. 2001; Navarete et al. 2015) of the source is aligned in a direction similar to that of *L* and *C* bands, suggesting the presence of a SE–NW outflow. Navarete et al. (2015) also detected knots that are typical of a bipolar jet with a similar orientation i.e. at a position angle PA~160°. Moreover, Jiang et al. (2001) detected a polarization disc that is oriented in a direction perpendicular to that of the outflow, suggesting a disc–jet case.

A12 G136.3833

G136.3833-A was detected at both *C* and *Q* bands but not at *L* band where the field rms is ~50 μJy beam^{-1}. It is a thermal radio source whose *C*–*Q* band spectral index α_{CQ} is ~1.22 ± 0.11. A non-thermal source B of spectral index $\alpha_{LC} = -0.68 \pm 0.08$ was detected approximately 6 arcsec to the west A at *L* band. The source whose position angle is 60 ± 12° at *L* band is elliptical at *L* band but irregular at *C* band. The IR nebula in the field is oriented in an EW direction (Skrutskie et al. 2006), just like the alignment of sources A and B (see Fig. A7). Both A and B have 2MASS counterparts at *K* band and B may therefore be a non-thermal lobe or a star.

A13 G138.2957

G138.2957, also known as AFGL 4029 (Ray et al. 1990), displays an extended morphology at *C* band but splits into B and C at *L* band. Both B and C are non-thermal lobes of flux densities 0.13 ± 0.04 mJy and 0.10 ± 0.03 mJy, respectively. Polygons whose sizes are equivalent to the size of the sources at *L* band were used to estimate their fluxes at *C* band. The flux of B and C at *C* band were determined to be approximately 0.07 ± 0.02 and 0.06 ± 0.02 mJy, respectively, giving them spectral indices of −0.46 ± 0.31 and −0.38 ± 0.33, respectively. Its spectral index map also display evidence of non-thermal emission, with some pixels having a non-thermal index of −0.6 ± 0.2. The central core of the source was not detected at *L* band. It appears to be located at the position of the peak emission at *C* band (Fig. 3). A polygon that is equivalent to the *C*-band contour of level 7 (80 μJy beam^{-1}), which encloses the peak emission, was used in estimating the flux density of the core at *C* band as 0.09 ± 0.01 mJy. A similar polygon was used at *L* band, approximating its peak flux at the frequency as <0.06 mJy. The fluxes suggest that the source has a thermal core of spectral index $\alpha > 0.69$.

The source drives an optical jet (Ray et al. 1990) whose position angle is comparable to that of *C*-band emission (~75°). Navarete et al. (2015) also mapped a bipolar outflow of position angle PA ~ 90 deg that appears to be associated with it. Kurtz, Churchwell & Wood (1994) and Carral et al. (1999) observed the source using B and D configurations of the VLA, estimating its flux density at 3.6 cm to be ~2.1 and 0.60 ± 0.12 mJy, perhaps signifying variability.

A14 G139.9091A

G139.9091A, also known as GL437S (Kumar Dewangan & Anandarao 2010), is a thermal radio source of spectral index $\alpha = 0.36 \pm 0.04$. It has a position angle of ~50 ± 8°, similar to the orientation of de Wit et al. (2009)'s mid-infrared emission. Similarly, Manjarrez, Gómez & de Gregorio-Monsalvo (2012) imaged it using archival data from JVLA's B, C, and D configurations at 3.6 and 2 cm getting a comparable position angle i.e. ~60°. Its flux densities at 3.6 and 2 cm are 1.5 ± 0.4 and <2 mJy, respectively, perhaps a sign of variability. Both infrared (Fig. A8) and CO (Gomez et al. 1992) emission of the field are aligned in a N–S direction; however, its 2.12 μm map (Davis et al. 1998) does not show evidence of outflow.

Apart from G139.9091A, an optically thin H II region of spectral index −0.11 ± 0.02, also identified as AFGL 437W (Manjarrez et al. 2012), was detected to the NW of A. It has flux densities of 19.0 ± 0.5 and 16.3 ± 0.4 mJy at *L* and *C* bands, respectively.

A15 G141.9996

G141.9996, also known as AFGL 490 (Davis et al. 1998), is an extended source that is largely elongated in an N–S direction (see Fig. A9.). Two lobes, B and C, of flux densities 0.06 ± 0.03 and 0.07 ± 0.03 mJy, respectively, were detected at *L* band but not at *C* band. The *L*–*C* spectral indices of B and C are $\alpha_{LC} < -0.51$ and <−0.63, respectively, suggesting that they are non-thermal lobes. The core, A, is thermal and is elongated in a direction that is similar to the alignment of A, B, and C, i.e. PA ~ 180°. Both CO outflow (Mitchell et al. 1995) and 2.12 μm emission (Davis et al. 1998; Navarete et al. 2015) maps of the field are oriented in a NE–SW
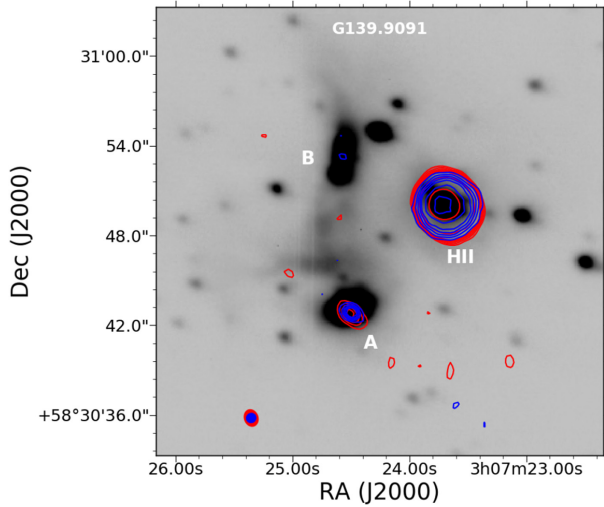
Figure A8. UKIDSS *K*-band map of G139.9091A field and overplots of *L*- and *C*-band contours shown in red and blue lines, respectively.
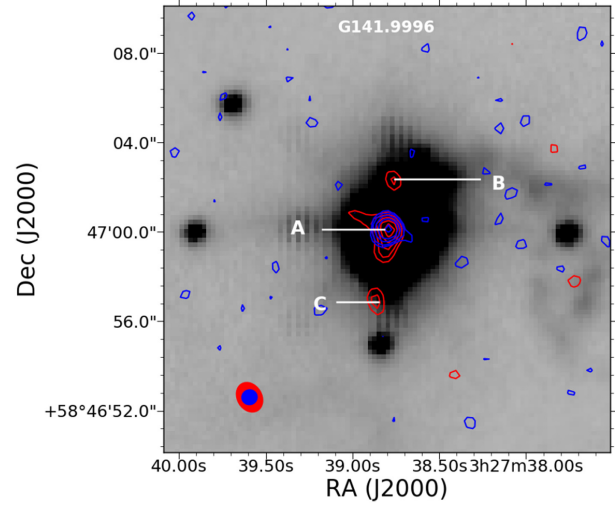

Figure A9. UKIDSS *J*-band image of G141.9996 shown in grey together with *L*- and C-band contours in red and blue, respectively.

direction. However, CS $J = 2 \rightarrow 1$ emission of the source has a positions angle of $-45°$ (Schreyer et al. 2002).

Also, an optically thin source of spectral index -0.06 ± 0.16 was detected approximately 13 arcsec away, at both bands. The source, located at α(J2000) $\sim 03^h27^m37\overset{s}{.}07$ $\delta \sim +058°46^m59\overset{s}{.}4$, has flux densities of 0.12 ± 0.03 and 0.11 ± 0.02 mJy at *L* and *C* bands, respectively.

This paper has been typeset from a TEX/LATEX file prepared by the author.